Fidelity of Biodegradable Patches Fabricated by a Custom-developed Low-cost 3D Bioprinter

Mikail Temirel, PhD

University of Connecticut, 2021

There is high demand in the medical field for biodegradable patches for a variety of applications such as wound healing. To keep the cost of the patches low, they would need to be fabricated using a high throughput, rapid method. Three-dimensional (3D) bioprinting is a promising technology that would make it possible to fabricate custom patches in such a high throughput, low-cost manner. Current commercial bioprinting systems tradeoff between resolution and throughput, and are inaccessible to researchers due to their high costs, ranging from $10k to over $200k.

Patch fidelity to the original design is an important aspect of the manufacturing process, ultimately influencing their functionality. A patch must be fabricated as close to its Computer-Aided-Design (CAD) model as possible, maintain its form for a certain period of time on the target tissue, then biodegrade. Deformation during the manufacturing, or biodegradation processes can limit the patch's performance. Fidelity on a 3D bioprinted biodegradable patch is analyzed in three dimensions: shape, mechanical and chemical fidelity. The former is concerned about preserving the shape of the printed filament and the accuracy of the patch structure. Mechanical fidelity is measures how well the patch preserves its structure under mechanical loads, such as those found once implanted in a body. Lastly, chemical fidelity is the ability of a patch to preserve its properties when exposed to chemicals such as body fluids and blood, such as during the degradation process. Assessing the fidelity and quantitatively characterization of a patch's properties are crucial for material development. This thesis focuses on developing a custom-made, low-cost and high-

Mikail Temirel

University of Connecticut, 2021

throughput hybrid printer for manufacturing 3D biodegradable patches, and providing thorough fidelity analysis of said patches through controlled experiments mimicking native tissue conditions.

First, a low-cost hybrid bioprinter with an inkjet and an extrusion print head was developed and implemented with the heads capable of printing gelatin methacryloyl and alginate respectively. The geometric accuracy of the printer was characterized. The printing and crosslinking parameters were then optimized to maximize the cell viability. Next, two novel shape fidelity experimental analysis techniques were developed, along with a mathematical model in supportive of one of the methods. These techniques are readily accessible and replicable, enabling rapid optimization of custom bioink formulations, accelerating the development processes. Finally, 3D bioprinted biodegradable patches were analyzed for shape, mechanical and chemical fidelity to improve their functionality. These patches are bioprinted using two custom hydrogels made of hybridized alginate and cellulose nanocrystal (CNC), or alginate and TEMPO oxidized cellulose nanofibril (T-CNF). Both formulations were ionically crosslinkable using calcium chloride. These hydrogels were rheologically characterized, and printing parameters using an extrusion printing head were tuned to optimize shape fidelity. Mechanical fidelity of patches was assessed by cycling loading experiments, emulating the stresses caused by human tissue motion. 3D bioprinted patches were exposed to a solution mimicking body fluid to characterize biodegradability of the patches. Biocompatibility of the hydrogels were tested by cell viability analysis.

Fidelity of Biodegradable Patches Fabricated by a Custom-developed Low-cost 3D Bioprinter

Mikail Temirel

B.Sc., Hitit University, 2011

M.Sc., Drexel University, 2015

A Dissertation

Submitted in Partial Fulfillment of the

Requirements for the Degree of

Doctor of Philosophy

at the

University of Connecticut

2021

APPROVAL PAGE

Doctor of Philosophy Dissertation

Fidelity of Biodegradable Patches Fabricated by a Custom-developed Low-cost 3D Bioprinter

Presented by

Mikail Temirel, B.S., M.Sc.

Major Advisor

_____

Dr. Savas Tasoglu

Associate Advisor

_____

Dr. Shararah Emadi

Associate Advisor

_____

Dr. Lakshmi Sreedharan Nair

Associate Advisor

_____

Dr. Ugur Pasaogullari

Associate Advisor

_____

Dr. Guoan Zheng

University of Connecticut
2021

ACKNOWLEDGEMENTS

I would like to express my appreciation and thanks to my Advisor, Dr. Savas Tasoglu for his support and guidance throughout my graduate studies.

Besides my advisor, I would like to thank to my thesis committee members Dr. Ugur Pasaogullari, Dr. Sharareh Emadi, Dr. Lakshmi Sreedharan Nair and Dr. Guoan Zheng for joining my committee and their feedbacks.

I also acknowledge the scholarship by Republic of Turkey Ministry of National Education (MEB) during my graduate studies at Drexel University and University of Connecticut.

I thank my friends in Connecticut for all their support, their kindness and the fun time. I have felt at home in the US with them.

I especially thank my parents, my beloved sister, and my brothers. Thank you all for being always with me, for supporting me spiritually, and for your continuous encouragement throughout my years of study.

Last but not the least; I would like to thank my loving and patient wife who never ceased her faithful support during my exhausting and grueling journey; especially in the moments when everyone else was unable to answer my queries. I could not have complete this dissertation without the support of her.

TABLE OF CONTENTS

LIST OF FIGURES

LIST OF TABLES

INTRODUCTION

Millions of people suffer from tissue loss or organ defects, contributing to over $400 billion per year total healthcare expenses in the United States[1]. Tissue engineering has the potential to help overcome these challenges through the development of regenerative tissues, autologous cells, biodegradable scaffolds, and various implants such as arterial reconstruction[2] and bone regeneration[3]. Multi-material and multi-functional biodegradable patch research is a promising field, It offers increased functionality, cost-efficiency, and production feasibility with organic and inorganic materials; moreover, they are biodegradable, meaning that they are gradually extinguished from the body after fulfilling their functions. Biodegradable patches have been used for a variety of reasons, including restoring function, facilitation healing, and replacing organs such as skin or tissues after injury or disease. Biodegradable patches have been used for different applications including wound healing[4], cardiac reconstruction[5], health monitoring[6], and drug delivery[7]. Their use in wound healing is particularly promising. The skin is the largest organ in the body and is an open door for potentially harmful impairments or injuries such as acute trauma, burns, surgical defects, or long-term diseases such as eczema and diabetes[4,8]. A skin injury larger than 4 cm will not heal without external support[9], often requiring donor skin; however, the availability of donor skin is limited. Biodegradable patches offer a robust alternative solution via composition of non-toxic and non-allergic materials.

The first biodegradable patches were single- or multi-layered patches with no spatial heterogeneity in planar material properties or functionality[10]. Recently, with the growth of wearable technologies and their emerging applications, electronics have been integrated

into patches and spatially heterogeneous material deposition has been achieved[6,8,7]. From this perspective, 3D bioprinting can be used for the high throughput fabrication of these patches via multi-material deposition without requiring manual handling or steps. Bioprinting can readily produce custom biodegradable patches that are compatible with specific native tissues, such as external blood vessels and bone, and has potential to engineer fully functional organs as well as patient-specific tissues. Furthermore, modern applications of patches, such as health monitoring, require complex electronic integration with electronic sensors[6], which can be achieved by 3D bioprinting at high throughput, potentially in a single step. Thus, 3D bioprinting technology is expected to be increasingly used to generate patches due to its ability to deposit multiple materials in a single step. However, most commercially available bioprinters are limited by the tradeoff between resolution and throughput; moreover, the bioprinters are expensive and, therefore, inaccessible, ranging from $10k to over $200k.

A patch must maintain its shape and structure for some time on the target tissue or organ, then biodegrade after fulfilling its role. Fidelity on a 3D bioprinting biodegradable patch is analyzed in three dimensions: shape, mechanical and chemical fidelity. The former is concerned about preserving the shape of a filament after deposition and the accuracy of the printed structure. The assessing the shape fidelity is required to estimate printing accuracy with respect to printing techniques, bioprinter type, and bioink materials. Mechanical fidelity is achieved if a patch implanted in a body preserves its structure under mechanical loads. Mechanical loading is an important design consideration; for example, patches have been proposed or developed to serve as pressure sensors on vessels[6] and organs, and as repair materials for cardiac reconstruction in patients with complex

congenital heart defects[5]. In tissues that undergo periodic dilation and constriction, the shape of the patch and its material properties, biodegradability, and electronic components may be affected. It is critical to ensure that a patch maintains its fidelity under the mechanical loading over the targeted time. Lastly, chemical fidelity is defined as the ability of a patch to preserve its properties when exposed to chemicals such as body fluids and blood. Depending on the target organ or vessel, patches are intended to stay in the body for various lengths of time. For instance, a patch for monitoring blood flow may stay on a vessel for twelve weeks[6], while a cardiac patch might remain on an organ for ten weeks[11]. In addition, patches are usually prepared at room temperature (22-26 °C) before being applied to the body (37 °C). This temperature difference can affect the fidelity of a patch. Therefore, patches can be exposed to the chemical deformation on the targeted organ once they are implanted to the body. It is also essential to ensure that a patch preserve its fidelity under the chemical exposition until it fulfills its role. It is critical to quantitatively characterize the mechanical and chemical fidelity to develop a new patch material.

To achieve high fidelity (performance) 3D bioprinting cell-laden patches, one of the most important factors is the hydrogel material (bioink). The hydrogel needs to have enough viscosity to preserve its shape after deposition, and must keep its shape post crosslinking. Bioprinting hydrogel has several requirements, including effective printability, biodegradability *in vivo*, and strong and elastic physical properties for mechanical loading[12]. Alginate is a widely used hydrogel material in bioprinting due to its low-coast, easy and rapid crosslinking with calcium chloride, innate biocompatibility, while maintaining high cell viability. Alginate, however, has several drawbacks to its use in

bioprinting, including low mechanical properties, low viscosity, slow degradation, and limited printability[13]. This limits its design and use in some applications that required mechanical loading, such as a cardiac implant. To counter this issue, other materials can be added to increase the viscosity and mechanical strength. For example, the structural fidelity of printing with alginate had been increased by blending the alginate with carbon nanotubes (CNT)[14], gelatin methacryloyl (GelMA)[15,16], hydroxypatite[13,17], and cellulose[18,19].

Cellulose nanoparticles are one of the most attractive co-materials for tissue engineering. Cellulous nanoparticles have several advantages including sustainability, biocompatibility, abundance, water-retention, and high chemo-mechanical properties[20,21,22]. Cellulous nanoparticles can also be found in different forms, including cellulose monocrystalline (CNC) which is used for many applications including reinforcing alginate-based hydrogels[23]. Another form is cellulose nanofibril (CNF) which is used to improve rheological and mechanical properties of pure alginate with respect to printability and structural fidelity[24]. Of particular interest is one form of CNF, TEMPO-mediated oxidation cellulose nanofibril (T-CNF), which shows excellent printability, mechanical strength, and viscosity within the ideal range[25].

In response to these factors, in my PhD study, I focused on to develop custom-made low-cost and high-throughput hybrid bioprinter and analyze the fidelity of 3D bioprinted biodegradable patches, including, shape, chemical, and mechanical fidelity under controlled conditions of mechanical loading and chemical exposition mimicking native tissue constraints.

In this regard, a low-cost hybrid bioprinter was developed using both inkjet and extrusion print heads, which are capable of printing gelatin methacryloyl (GelMA) and alginate, respectively (Chapter 1). It is capable of printing of custom designs and structures by using a CNC XYZ stage as a platform. Bioink is deposited from a reservoir of biomaterial through one of the two print heads and onto the printing bed. The spatial precision of the individual drops were characterized from the inkjet print head, which are used to create the desired density and infill of the printed structure. Then, the distribution of light was measured to cure the deposited GelMA while also preserving the viability of cells suspended in the hydrogel. In addition, the filament and channel diameter of the extruded prints were characterized with respect to the print head speed for the extrusion print head. The viability of cells printed from both print heads was characterized to optimize the printing parameters. The results demonstrate the feasibility of the proposed hybrid.

At the next step, assessing the printability and shape fidelity of alginate based bioink was quantitatively performed with two approaches (Chapter 2). First, evaluating the filament collapse to estimate the filament deformation when printing over supports of varied spacing, temperature, and alginate concentration. A theoretical model was developed to predict the Young's modulus of the filament as a function of its radius. Finite element analysis was performed to validate the theoretical model. Alginate's poor printability was then improved by adding varied concentrations of gelatin. Characterization of the rheological properties of alginate-gelatin blends as viscosity, storage-loss modulus, mechanical characterization of 3D printed, and crosslinked samples through mechanical loading were performed. Then, 2-layer and 6-layer grid patterns were printed with alginate-gelatin blends and pore area between the grid patterns was measured after

printing, crosslinking and 2 day incubating in order to determine best shape fidelity, and effect of incubation on shape fidelity. The biocompatibility of these proposed bioink blends was tested with cell viability test.

As a final application, 3D bioprinted biodegradable patches to be implanted on real human tissue were analyzed for shape, mechanical and chemical fidelity to improve their functionality (Chapter 3). These patches are bioprinted using two hybrid hydrogels made of alginate-cellulose nanocrystal (CNC) and alginate-cellulose nanofibril (CNF) ionically crosslinkable using calcium chloride. These hydrogels are rheologically characterized and printing parameters, including, print speed and nozzle pressure using an extrusion printing head are tuned for improved shape fidelity. Also, mechanical fidelity of patches was assessed through cyclic loading experiments that emulate human tissue motion. Lastly, 3D bioprinted patches were exposed to a solution mimicking the body fluid to characterize the biodegradability of patches at body temperature up to 30 days. In addition to the biodegradability test, the morphological structure of patches was characterized through the scanning electron microscopy images to observe the effect of degradation on the microstructure of them. Biocompatibility of the hydrogels were tested by cell viability analysis using NIH 3T3 mouse fibroblast cells.

1. CHAPTER 1: Development and characterization of a low-cost 3D bioprinter

Introduction

With an increasing demand for readily available, scaled-up, biomimetic tissues and organs, bioprinting technologies are advancing rapidly. Applications within tissue engineering and regenerative medicine include creating organ-on-a-chip devices for medical and drug discovery research[26,27] and replicating disease tissues such a tumors to better understand the disease process[28,29] regenerating human tissues to replace those which are damaged or diseased[30,31,32], and conducting stem-cell research[33]. Of particular interest are methods to construct various "bioinks" into complex three-dimensional (3D) designs, including patterning multiple types of bioinks in a single construct, to closely mimic the *in vivo* micro-environment[34,35,36,37,38]. However, while the spatial distribution of cells is critical to direct cell- and tissue-level behavior, it remains a significant challenge to create such complex constructs in a high-throughput manner. As an emerging solution, bioprinting is an attractive technique for high-throughput, repeatable, and precise construction of cell-laden structures on the micro- and macroscales[39]. However, most commercially available bioprinters are limited by the tradeoff between resolution and throughput; moreover, the bioprinters are extremely expensive (and, therefore, inaccessible), ranging from $10,000 to over $200,000.

The foundational concepts behind bioprinting are commensurate with those of the more common 3D printing: material is added to the print in progressive layers to form 3D objects. Bioprinters must be designed to be compatible with cell-laden bioinks, which places limitations on the heating, forces applied in the printing nozzle, and other parameters due to the limited range of biocompatible materials available as well as the need to maintain cell viability throughout the process. A range of bioprinters have been

proposed which achieve this with various bioinks, including most ubiquitously extrusion-based printing using filaments, inkjet printing of liquid droplets, and laser-assisted bioprinting[40]. While inkjet-based bioprinting general offers superior resolution, it is a challenge to implement it with certain biomaterials because it is only compatible with low-viscosity bioinks.

Hydrogels have been shown to serve as an excellent extracellular matrix (ECM) to facilitate cell growth[41,42]. One ECM scaffold which shows great promise is gelatin methacryloyl (GelMA)[43]. GelMA is an inexpensive and cell-responsive biomaterial naturally derived from denatured collagen (a very common structural protein in the body) and chemically modified with a methacrylate group. Cells have been shown in many studies to survive, grow, and even form functional 3D networks within scaffolds of various materials, particularly those made of naturally derived materials like GelMA and alginate[13].

Bertassoni et al. implemented a block-based bioprinting technique to print with GelMA by crosslinking and extruding 30 mm by up to 65 mm building blocks one at a time[44]; however, this approach is limited by the block size. An extrusion-based approach developed by Kolesky, et al. used a fugitive ink, pluronic F127, as a support material into which the GelMA matrix was printed and photocrosslinked and subsequently removed by cooling to 4 °C[45]. Zhu, et al. used a stereolithography-based bioprinter to encapsulate neural stem cells in a GelMA-based bioink with graphene nanoplatelets[46]. Inkjet-based bioprinters have been implemented with a limited range of bioinks, and Gao et al. used a blend of polyethylene glycol and GelMA to tune the bioink properties to be compatible with an inkjet printer. However, to our knowledge, inkjet bioprinting has not been applied

successfully to pure GelMA, which is desirable to take full advantage of the cell-supportive properties of the material.

Alginate is another biomaterial that has been studied extensively[47], particularly for bone[48] and cartilage[48] tissue engineering. While mammalian cells do not attached to unmodified alginates, the structure can be readily modified with domains such as Arginylglycylaspartic acid (RGD) to facilitate cell attachment and growth[47]. It is readily crosslinked by mixing with calcium (such as calcium chloride). A few bioprinters compatible with alginate have been proposed. Park et al. studied different compositions of alginate bioinks, finding that high- and low-molecular-weight alginate can be mixed to facilitate cell growth[49]. Alginate is often blended with other materials to improve its printability and cytocompatibility. For example, Schutz et al. added 3% methylcellulose to improve the viscosity and thereby facilitate deposition[50].

Here, we propose a custom bioprinter leveraging both inkjet and extrusion printing (Fig. 1.1) and demonstrate their abilities to print cell-laden GelMA and alginate, respectively. It is capable of printing of custom designs and structures by using a CNC XYZ stage as a platform. Bioink is deposited from a reservoir of biomaterial through one of the two print heads and onto the printing bed.

The inkjet head relies on photocrosslinkability and temperature-dependent viscosity transition of GelMA. Upon exposure to light in the presence of a photoinitiator, these methacrylate groups crosslink with one another, forming a structural network on which cells can grow. This feature offers temporal control over the material properties of the bioink simply by applying UV light. Thus, GelMA can be compatible with inkjet printing as a low-viscosity bioink before crosslinking, then be imparted with the mechanical

properties needed to maintain the printed structure after crosslinking. Photocrosslinking is mediated by a photoinitiator such as Irgacure 2959, which initiates crosslinking in the far UV light range (280 nm, although longer UV wavelengths up to 365 are often used with slightly lower efficiency) or lithium phenyl-2,4,6-trimethylbenzoylphosphinate (LAP), which initiates crosslinking in the blue light range (405 nm)[51]. It should also be noted that LAP has been shown to have a lower cytotoxicity than some other photoinitiators. We also take advantage of the documented temperature-dependent change in viscosity[45]: the shear elastic modulus of uncrosslinked GelMA changes from above 10^4 Pa at 4 °C to approximately 10^{-2} Pa at 37 °C. Similar to the application of light, the application of heat is controlled such that the bioink is heated in the printer head to attain a low viscosity, then as it cools on the printing platform, it attains a higher viscosity.

In addition to the inkjet head, the extrusion-based printing head is comprised of a coaxial printing head, which is a widely reported extrusion method[37,52,53,54,55]. Alginate is co-extruded with a stream of calcium chloride in the center to crosslink the structure. While this extrusion-based printing is lower in resolution, as the resolution is mainly limited by the width of the extruded filament, it provides a relatively high-throughput compared to inkjet printing. Thus, the hybrid bioprinter is expected to leverage the unique benefits of both extrusion and inkjet printing.

Herein, we characterize the spatial precision of the individual drops from the inkjet print head, which are used to create the desired density and infill of the printed structure. We then measured the distribution of light to cure the deposited GelMA while also preserving the viability of cells suspended in the hydrogel. In addition, we characterize the filament and channel diameter of the extruded prints with respect to the print head speed for the

extrusion print head. The viability of cells printed from both print heads was characterized to optimize the printing parameters. The results demonstrate the feasibility of the proposed hybrid droplet-and-extrusion-based bioprinter.

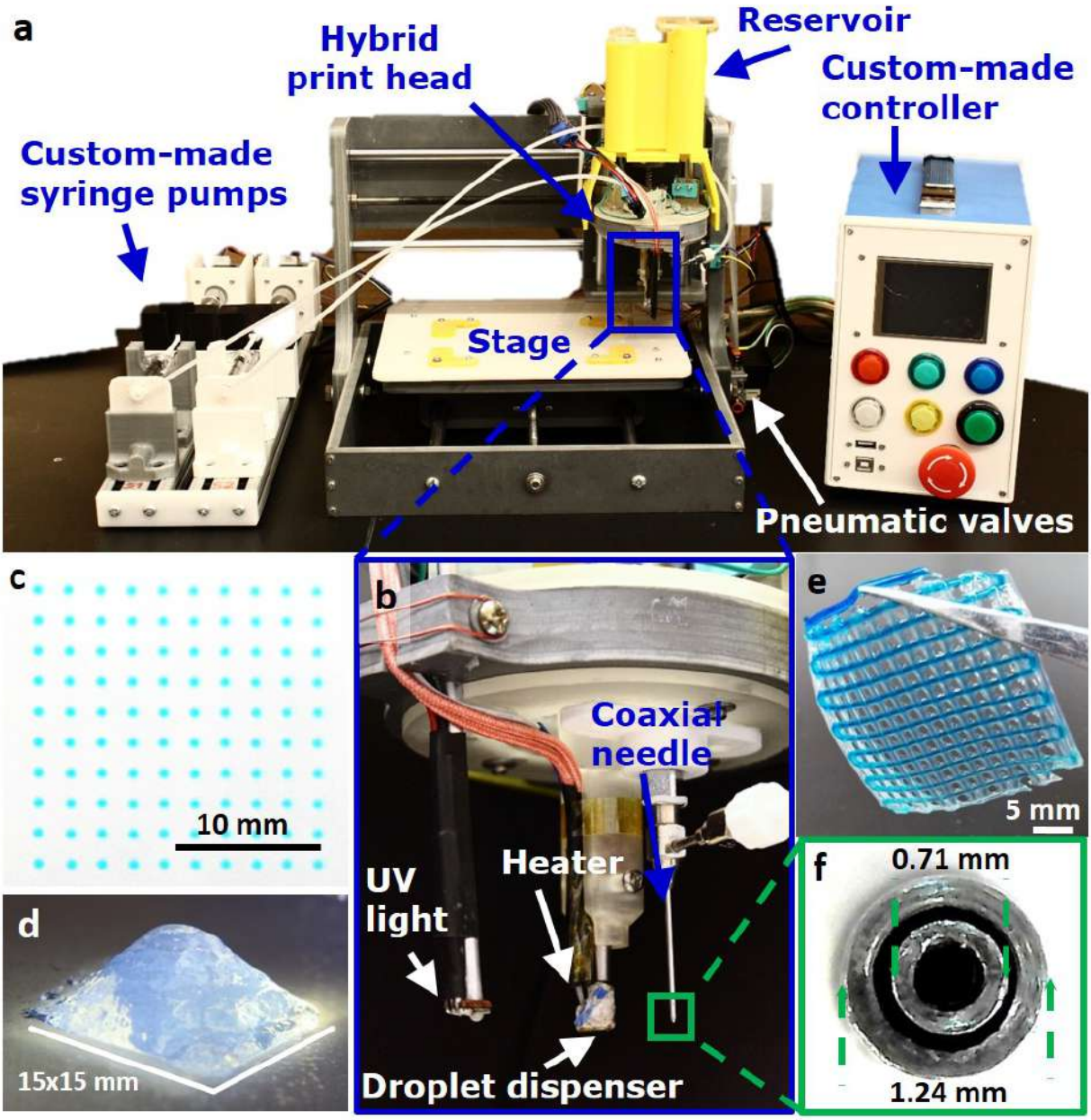

Figure 1.1. (a) *Overview of the proposed hybrid bioprinter and* ***(b)*** *a close-up of the printing heads including a droplet dispenser for inkjet printing, a UV light for crosslinking the bioink following deposition, and a coaxial needle for extrusion printing.* ***(c–d)*** *Demonstration of the inkjet printing showing* ***(c)*** *individual droplets and* ***(d)*** *a 3D 21-layer pyramid.* ***(e–f)*** *Demonstration of extrusion printing showing* ***(e)*** *an image of a printed mat*

*where the second layer is printed perpendicular to the first and dyed blue for better visualization and **(f)** a close-up of the printing head with two inputs for alginate and $CaCl_2$.*

Methods

Mechanical design

The bioprinter (Fig. 1.1a) is based on a gantry-type three-axis CNC stage (2020B, Konmison, China) where the X and Z-axis are on the gantry and the Y-axis is on the worktable. A custom head was designed (Fig. 1.1b) to hold the 405 nm near-UV led (Luminus Devices Inc., MA, US), a submicroliter dispensing valve G150-G1501000 (TechElan llc, NJ, US), a coaxial syringe tip (Rame-hart Instrument Co., NJ, US), and a custom syringe holder. For the droplet printing, a 90 psi pressurized air source was regulated to the desired pressure (15–45 psi) using a miniature air pressure regulator PPR2-N02BG-4 (PneumaticPlus, CA, US) and connected to the syringe through a solenoid valve VQ110U-5M (SMC, Tokyo, JP). For the extrusion printing, two custom syringe pumps were designed and connected to the coaxial needle tip. When the printer is in operation, three motors (namely x- y- and z-directions) were used to control the motion of the syringe on three directions. To protect the dispenser head from unexpected impacts, micro switches (uxcell, Hong Kong, China) detect if the nozzle hits an obstruction and automatically stops movement. The sample (such as GelMA) loaded in the syringe was ejected from the nozzle followed by curing by the UV light (Fig. 1.1b) for droplet-based printing, whereas alginate cured chemically for extrusion-based printing.

Electrical design

The movement of the axis was controlled with an Osoyoo MKS Gen 1.5 3D printer controller (Pinetree Electronis Ltd, Canada) loaded with the open-sourced Marlin

firmware. The solenoid valve was controlled with the same board through a MOSFET driver board (FlamingoEDA, Beijing, China).

Production and modification of G-Code

The designs for 2D printed objects were created with a custom MATLAB (Mathworks, MA, US) GUI, where the user can select from available patterns, modify their parameters and export it as g-code. The designs for 3D printed objects were created in SolidWorks 2017 (Dassault Systèmes SolidWorks Corp., Waltham, MA), a professional computer aided design software, and saved as an STL file. Slic3r (version 1.2.9 stable), a free open sourced 3D printing processing software, was used as the slicing engine to produce the g-code file for 3D STLs. The g-code files either from the GUI or from the Slic3r were then loaded into Repetier-Host (version 1.6.2), a free 3D printing software interface (Hot-World GmbH & Co. KG, Willich, Germany) that controls the bioprinter connected to the computer through a USB port.

Bioink preparation

GelMa was synthesized as described in literature[43] and prepared at a final concentration of 50 mg/mL in PBS (phosphate buffered saline) with 0.5% LAP (Biobots, Philadelphia, PA, US) at 37 °C. The bioink was filtered through a 0.2 μm sterile filter before use to remove the particles that may clog the printhead. National Institutes of Health (NIH) 3T3 mouse fibroblast cells (ATCC, US) were then trypsinized to prepare a single-cell suspension and added to the bioink at a concentration of approximately 3 million cells/mL immediately before printing. The bioink was protected from light during preparation to avoid unintended crosslinking.

Sodium alginate powder (Sigma-Aldrich, US) was added to PBS at a concentration of 2%, 4%, 6%, or 8% (w/v) and vortexing for one minute at 3400 rpm. The solution was then kept in the oven at 37 °C overnight to dissolve the alginate. The bioink solution was filtered through a 5 µm sterile filter and mixed with cells as described for GelMA. The bioink was then loaded into 10 ml syringes. The ionic cross-linker, calcium chloride ($CaCl_2$) (Sigma-Aldrich, US), was dissolved in PBS at 2% (w/v) by mixing on a vortex at 3400 rpm for one minute and loaded into another 10 ml syringe.

Printing parameters

For inkjet-printing, the prepared bioink was loaded into the sterilized reservoir. A pressure of 10 psi was applied to the bioink reservoir and 24 volts was applied to the solenoid for 56.25 µs to form each drop as the print head moved along the x- and y-axes. Each layer was crosslinked immediately after printing and once the entire print was deposited and crosslinked, PBS was applied immediately. For prints with encapsulated cells, the prints were subsequently washed twice with cell media at 10-min intervals and then incubated in complete cell media at 37 °C with 5% CO_2.

For the spatial accuracy characterization, GelMA with fabric dye was used as the bioink to create a 20 x 20 mm grid pattern. The printed pattern was imaged with a camera and image processing was done through MATLAB to detect the center points of each dot and calculate the deflection of the dots as compared to their expected location.

The exposure pattern of the UV curing light was characterized by exposing SunArt Paper (TEDCO Toys, USA) for various times: 1, 10, 20, and 30 s. The SunArt Paper is developed by UV light according to the amount of exposure received, similar to the process by photography film is exposed. The curing light was positioned 5 mm above the

paper during exposure to mimic the height between the light and well plates used during printing. These exposed papers were then digitalized using a flatbed scanner and analyzed in MATLAB to determine the normalized intensity and exposure pattern.

For extrusion-printing, the prepared syringes with the bioink and 2% $CaCl_2$ were placed on the two different syringe pumps and the flow rates were set to 0.15 and 0.1 ml/min, respectively. The nozzle speed was set to 6 mm/s. The bioink was deposited on glass slides in a grid pattern. After printing, the samples were transferred into a well plate. Warm PBS was applied immediately followed by two washes with cell media and the samples were finally incubated in cell media.

Viability characterization

To characterize the cell viability and proliferation of inkjet-printed cells, immunocytochemistry of proliferating cells was accomplished by staining with DAPI (blue), Ki67 (red), and Phalloidin (green). The cell encapsulating hydrogels were fixed with 1% paraformaldehyde for 1 h at room temperature and subsequently washed. The cells were permeabilized with 0.3% Triton-X 100 (Sigma), in 1% BSA (Sigma), for a minimum of 1 h at room temperature. First, the hydrogels were stained with Rb mKi67 (Ab16667, Abcam) overnight at 4 °C. After washing, the hydrogels were incubated with secondary antibody goat anti rabbit Alexa Fluor 564 (A11011, Invitrogen) for 2 h at room temperature. Actin cytoskeletons were visualized with phalloidin, while DAPI was used for nuclear counter staining. After washing, the hydrogels were observed and imaged under a fluorescent microscope (Zeiss AXIO).

For cell viability, calcein AM (which stains live cells green) and ethidium homodimer-1 (EthD, which stains dead cells red) stains were used (Life Technologies). The stained cell

were then observed under a fluorescence microscope. The constructs were washed once with PBS and then a solution of 1:2000 calcein and 1:500 ethidium homodimer in PBS was applied. Each sample was thoroughly covered with the staining solution and then incubated for 15 minutes. After a 15 min incubation period at room temperature, the staining solution was aspirated and all the samples were washed with PBS for imaging. Images were captured from six different focal planes over a z-axis range of 250 μm in different areas of each print.

To quantify the cell viability, the six images were combined into a z-stack and the maximum value of each (x,y) pixel across all six planes was used to create a z-projection image for each channel separately. From each image, the “find maxima” function in ImageJ[56] was used with a noise tolerance value of 20 to identify local maxima in the image; each local maximum in the green-channel (calcein) image was taken as a live cell and each local maximum in the red-channel (EthD) image was taken as a dead cell. Then, the viability in each image was calculated as (live cells)/(dead cells+live cells). The average viability for each crosslinking time was taken as the total number of live cells divided by the total number of cells (live and dead) counted across several images from two different prints. The composite images shown are pseudo-colored to show both calcein and EthD staining in a single image.

Results

Spatial accuracy with inkjet printing

Spatial resolution in this system depends on both the droplet size and where the droplets are deposited by the printer head. Droplets are formed by the solenoid-driven dispensing valve. The dispensing valve is positioned within a solenoid, which acts as an

electromagnet to control the dispensing valve. When a voltage is passed through the solenoid, the induced magnetic field causes the dispensing valve to open. By controlling the duration of time that the dispensing valve remains open and the pressure at which the bioink is supplied to the dispensing valve, the droplet formation was manipulated. Once deposited, each droplet (created at 10 psi and 56.25 μs timing value) spreads to a diameter of approximately 531.71 ± 48.87 μm as shown in Fig. 1.2a. The deflection of each dot relative to its expected position is characterized by printing a grid pattern and comparing the X- and Y-deflections of these droplets relative to the intended positions (Fig. 1.2b). It is seen that the standard deviation is 0.0568 mm and 0.0624 mm for X- and Y-axis, respectively. To check the accuracy of this test method, the same procedure is repeated with an office laser printer. The deflection of a reference pattern printed using a laser printer returned a standard deviation of 0.0440mm and 0.0437mm for X- and Y-axis. With the resolution of 45 pixels per millimeter for the imaging setup, the standard deviation of the bioprinter was within the range of 1- 2 pixels.

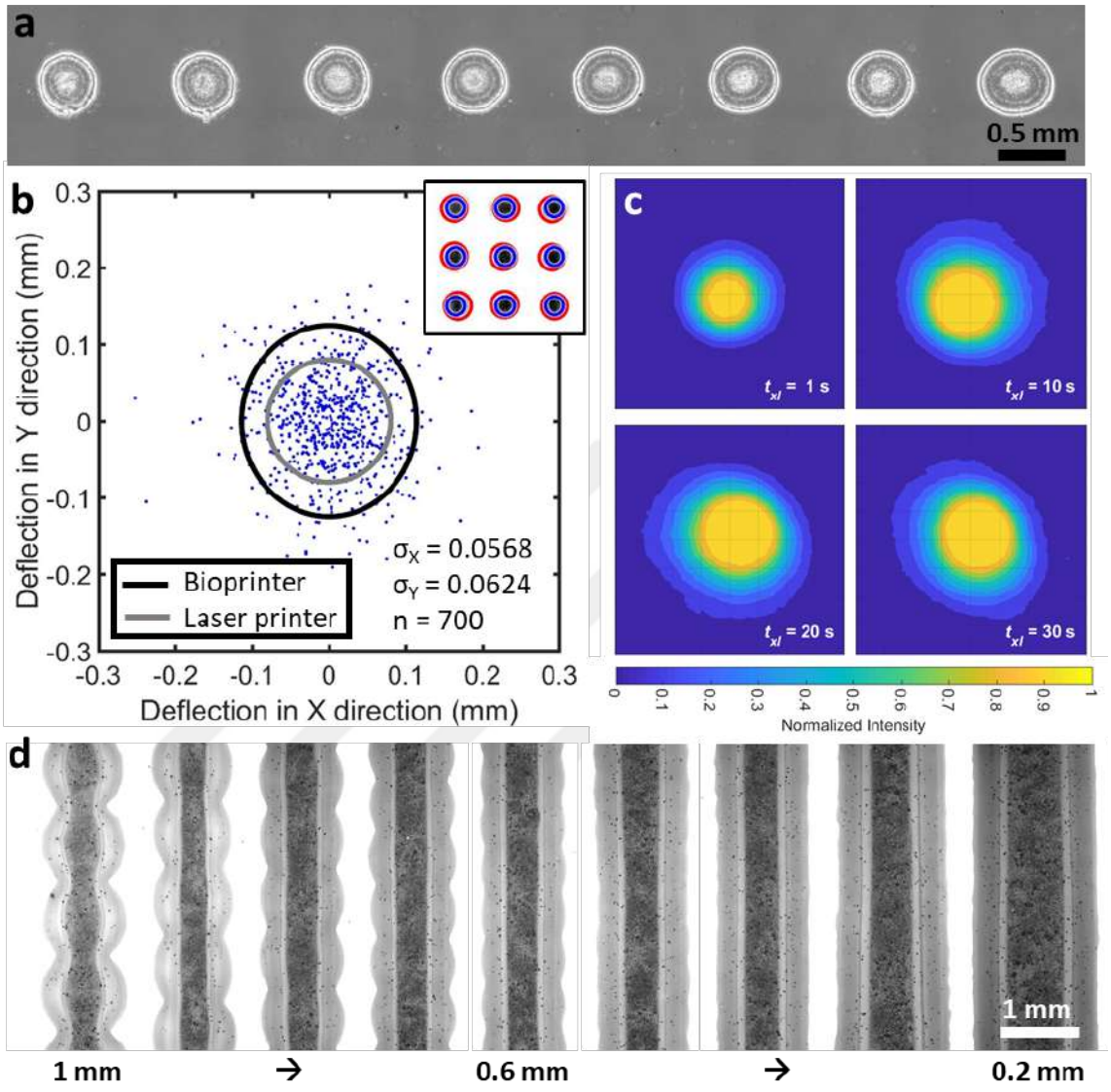

Figure 1.2. (a) *Close-up image of droplets formed by the solenoid valve at the chosen printing parameters.* ***(b)*** *The deflection in the x- and y-direction between the intended and actual droplet positions detected using image processing as shown in the inset at the top right; the 2-standard deviation ellipse is shown relative to the accuracy of a laser-printed pattern.* ***(c)*** *Light distribution patterns of the curing light for various exposure times. Clockwise from upper-left: 1 s, 10 s, 20 s, an 30 s exposure times. All exposures show a bullseye light distribution pattern. Full intensity UV exposure occurred within a 10 mm diameter at 1 s exposure, while for exposures of 20 s and greater experienced a 20+ mm diameter region of full exposure.* ***(d)*** *Inkjet-printed lines with varying droplet spacing's.*

Light distribution in the build area

The light exposure across the build area influences how the print will be crosslinked and therefore defines the build area. The intensity of the UV light output was tested by using an OmniCure radiometer (Model No. R2000, Lumen Dynamics Group Inc). The measured power output was 317 mW/cm2. The results of the SunArt Paper showed a bullseye-like (concentric circles) exposure pattern for all exposure times tested, as seen in Fig. 1.2c. For the 1-second exposure, the area of full intensity was limited to a circle of approximately 10 mm diameter, while a diameter of 25 mm received at least 50% UV exposure. As the exposure time increased, the area of exposure can be seen to increase up to 20 seconds, at which point the exposed area seems to plateau. For the 30-second exposure time, the area of full intensity was approximately 23 mm in diameter, and the 50% exposure region was approximately 35 mm in diameter.

Droplet spacing for inkjet printing

Because the bioink is deposited as droplets in inkjet printing rather than as a continuous filament, it was necessary to optimize the spacing between the droplets to obtain a continuous line. Several different droplet spacings were tested in the range of 0.2–1mm as shown in Fig. 1.2d. When the droplet spacing was decreased to 0.6 mm, the droplets began to merge into a line; however, further decreasing the droplet spacing resulted in the deposition of additional bioink per unit length of the printed line, resulting in spreading of the material over the surface and thickening of the line, which would negatively impact the spatial resolution of this printing process. Therefore, a droplet spacing of 0.6 mm was selected and used herein.

Nozzle speed for extrusion printing

In order to choose the optimum nozzle speed for the extrusion printing, the print head speed was characterized in terms of channel and filament diameters. We took the flow rate constant that was 0.15 ml/min for alginate and 0.1 ml/min for calcium. Two alginate concentrations of 4 and 6% w/v were tested with constant $CaCl_2$ concentrations of 2% w/v. 5 cm line was printed on a glass with varying print head speeds from 1 mm/s to 7 mm/min. Blue dye was injected to the channel via a 30G syringe needle to make the channel visible. Then images were taken by Canon camera for all speeds. Fig. 1.3a shows the effect of nozzle speed on the channel and filament sizes. At low speeds, the channel is noticeably wavy with accumulation of extra material. When the speed increases, the shape of channel obtains the desired straight form and its diameter decreases slightly. Fig. 1.3b shows the quantitative result of speed test for two alginate concentrations. The channel diameter does not significantly change for either concentration, while the filament diameter decreases with increasing nozzle speed. For low speeds, the hollow channel has a large wall thickness because the $CaCl_2$ crosslinks the alginate immediately when it exits the needle. The $CaCl_2$ then diffuses outwards from the center, resulting in a larger wall thickness for lower speeds since there is more time for the diffusion to occur. Moreover, there was a slight difference in the filament diameter between 4% and 6% alginate concentrations for low speeds. This may be caused by the higher viscosity of 6% alginate preventing the diffusion of $CaCl_2$. In conclusion, the 6 mm/s nozzle speed was chosen as an optimum speed in terms of the channel diameter, filament diameter, and wall thickness.

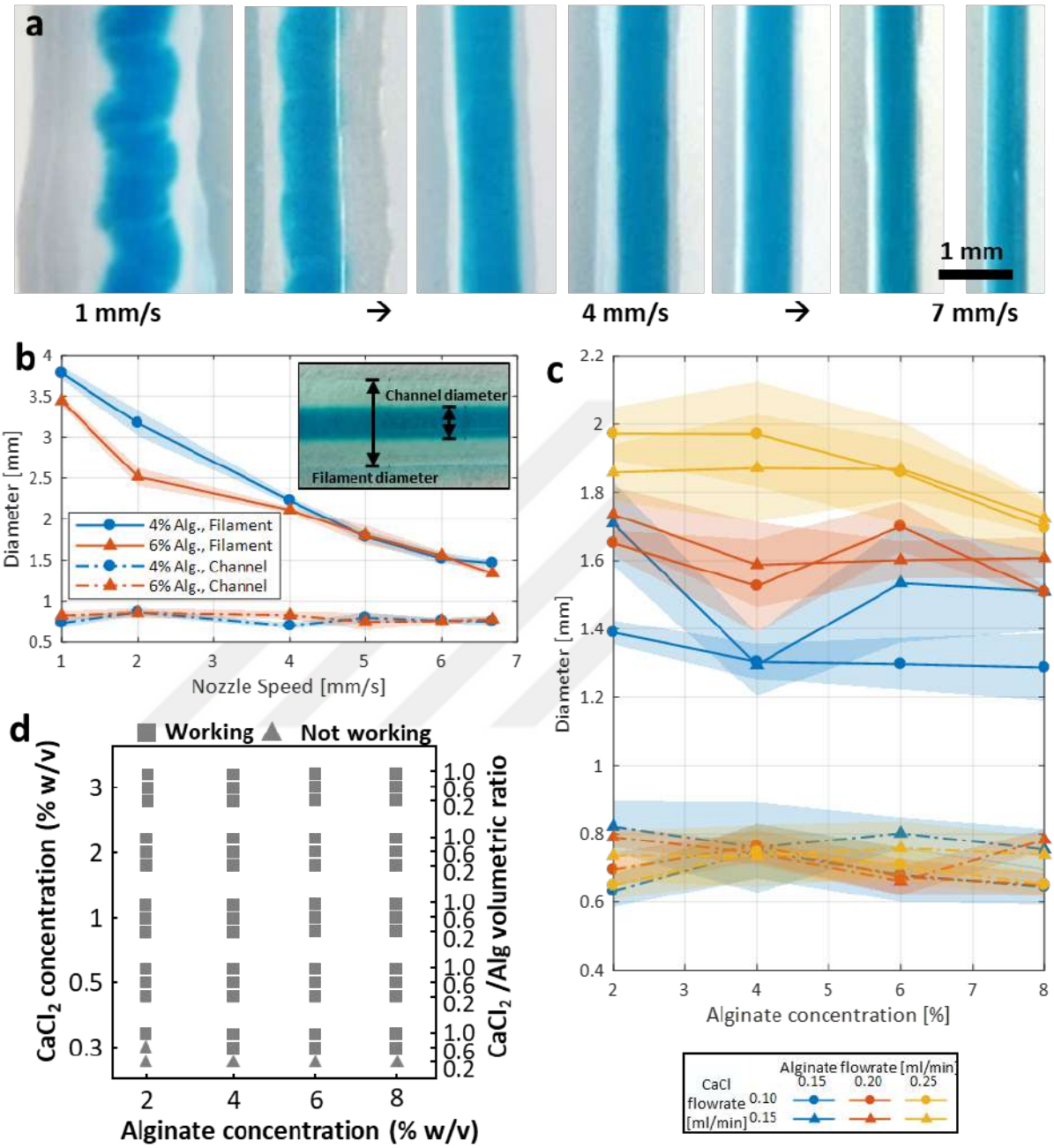

Figure 1.3. Characterization of alginate bioink and coaxial extrusion print head. (a) *Lines printed by extrusion at various print head speeds, showing the effect of the head speed on the filament and channel diameter.* ***(b)*** *Quantitative results of speed test that shows the effect of nozzle speed on the filament and channel diameter for two different alginate concentrations.* ***(c)*** *Alginate concentrations versus filament and channel diameter with different feeding rates.* ***(d)*** *Printability with several possible combinations of $CaCl_2$ and alginate concentrations that can be used to obtain effective prints.*

Alginate and $CaCl_2$ flow rates for extrusion

Fig. 1.3c shows the effect of alginate concentration on the channel and filament diameters for varying $CaCl_2$ flow rates at constant nozzle speed of 6 mm/s and constant 2 % w/v $CaCl_2$ concentration. As seen in the speed test, channel diameter did not have significant changes with varying alginate concentrations from 2 to 8 % w/v. Furthermore, alginate and $CaCl_2$ flow rates did not affect the channel diameter significantly, evidenced by the overlapping error bars all alginate $CaCl_2$ flow rates. However, filament diameter slightly changes with alginate concentrations and flow rates. 2 % alginate has larger filament diameter in all flow rates because of its low viscosity. It spreads out more when the alginate is deposited from the nozzles as compared to the higher viscosities. The diameter slightly decreased for 8% alginate due to the high viscosity which prevents spreading. Moreover, filament diameter increases with increasing of the alginate flow rate due to the deposition of more bioink. The filament diameter was not significantly affected by the $CaCl_2$ concentration. For all plotted values, each data points represents the measurements of three repetitions.

Fig. 1.3d shows a performance chart for the extrusion process (i.e. depositing $CaCl_2$ through the 22G inner nozzle while depositing alginate with via the 18G outer nozzle). The successful formation of the hollow channel was observed with certain combinations of alginate and $CaCl_2$ concentrations and certain volumetric ratios of these components as indicated by the squares in the figure. Moreover, it was found that the 8% w/v alginate concentration is the maximum concentration compatible with the needle sizes used; higher concentrations are not compatible due their high viscosity. However, the use of

lower alginate concentrations is preferred as the 8% alginate solution could not be sterile filtered due to its high viscosity, which presents a high risk of contamination.

Cell viability

For the inkjet-printed cells, the crosslinking time was varied to determine its effect on cell viability. As a control, the cell viability within precursor GelMA solution without being printed was used. The hydrogel was not sufficiently crosslinked and dissolved during the incubation period with crosslinking times lower than 20 s. However, with crosslinking times between 20 and 30 s, the cell viability did not vary significantly. For longer crosslinking times, cell viability decreased. With 25 s or more crosslinking time, there is a notable decline in cell viability along the edge of the construct and the width of this reduced viability region on the edge expands as the crosslinking time decreases, which gives rise to the decreasing trend in viability measured in these gels. This may be attributed to the stresses exerted on the cells as the hydrogel meets the build platform and spreads, due to drying of the gel between when the droplets are deposited and PBS is added, or because excess UV light is focused on the cells in this region as the layer of bioink is thinner. With the crosslinking time optimized, the cell viability and proliferation were studied. Fig. 1.4a–c shows fluorescence images of inkjet-printed NIH 3T3 mouse embryonic fibroblast cells in GelMA seven days after bioprinting. The viability was quantified over the course of the week, where the viability on day 0, 1, 2, 3, and 7 was 92%, 90%, 87%, 91%, and 93%, respectively, as summarized in Fig. 1.4d.

For extrusion-printed alginate constructs, the alginate concentration was varied to characterize the effect of the alginate concentration on the cell viability with a constant calcium concentration of 2% (w/v). The cell viability results for varying alginate

concentrations are summarized in Fig. 1.4f. The highest viability of 88% was observed in 4% alginate on day 3, decreasing slightly to 80% on day 7, possibly due to competition for oxygen and nutrients. The fluorescence image of extrusion-printed cells showing the cell viability after three days in 4% alginate is shown in Fig. 1.4e. For 6% alginate, the viability was 64% at day 3 and decreased to 47% viability at day 7. The decreases might be caused by contamination. The viability was around 50% on days 3 and 7 in the 2% and 8% alginate prints. The low viability observed with the low alginate concentration can be attributed to the weak crosslinking and corresponding degradation of the construct, as well as the low structural integrity of the 2% alginate prints. The low viability observed with higher alginate concentrations can be attributed to the high viscosity, which results in high pressures inside the reservoir during printing, which can stress the cell membrane and result in cell death. Thus, the optimum alginate concentration was concluded to be 4% in terms of both the resulting viability and the printability due to the viscosity.

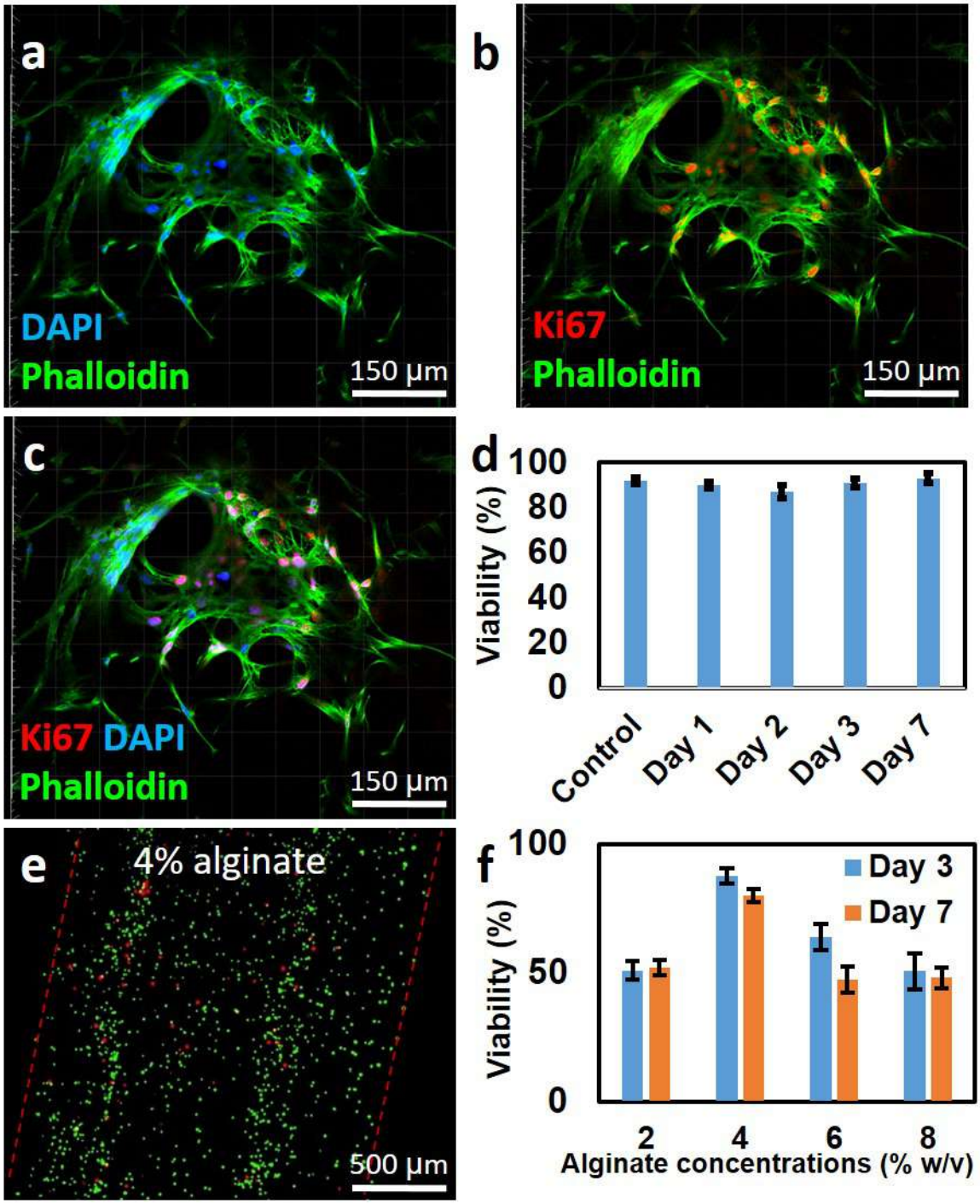

Figure 1. 4. Characterization of cell viability in inkjet-printed GelMA and extrusion-printed alginate constructs. (a–c) *Fluorescence images of inkjet-printed National Institutes of Health (NIH) 3T3 mouse embryonic fibroblast cells in GelMA showing the cell viability after seven days. The constructs are stained with DAPI (blue), Ki67 (red), and Phalloidin (green).* ***(d)*** *Viability of inkjet-printed cells over seven days: 92%, 90%, 87%, 91%, and 93% for control (day 0), day 1, 2, 3, and 7, respectively.* ***(e)*** *Fluorescence image of extrusion-printed cells showing the cell viability after three days in 4% alginate. The image shown is the Z-axis projection of six two-channel fluorescence images taken over*

the entire height of the constructs. ***(f)*** *Quantification of the cell viability after seven days with a range of alginate concentrations demonstrating that 4% alginate results in the highest cell viability.*

Characterization of 3D fabrication

3D patterns were fabricated by successive layers of printing followed by curing. To demonstrate the 3D printing capabilities of the proposed bioprinter, the University of Connecticut (UConn) wordmark was 3D printed using the inkjet head, as shown in Fig. 1.5f. Each layer was first printed then cured for 20 s under the near-UV light, and then the next layer is printed on top; this was repeated several times to form the finalized print. The multi-layer 15 mm square-based pyramid print in Fig. 1.1d was printed with 21 layers. Fig. 1.5b shows how the layers are constructed using the extrusion print head. The first layer is undyed while a blue food color was added to the second layer for contrast. It shows that fluid can pass through the hollow channel.

To quantify the approximate layer heights of the 3D prints, successive layers of a solid/filled 1 cm square were printed and imaged. Images were captured during the process (Fig.1.5a shows the inkjet prints and Fig. 1.5b shows the extruded prints). The images shown were processed to determine the total height of each print (in microns). The height of each print was measured both immediately after printing and after swelling in PBS. The inkjet and extruded print heights plotted in Fig. 1.5c and d, respectively, show that there is a near-linear trend in the as-printed height although there was slightly more variation in the post-swelling heights. Accordingly, it can be concluded that each inkjet layer has a relatively constant printed height of 16.5 ± 2.3 μm while each extruded layer has a printed height of 700 ± 83 μm.This further highlights the higher resolution that is

possible with the inkjet print head while also demonstrating the higher throughput that can be achieved with the extrusion head.

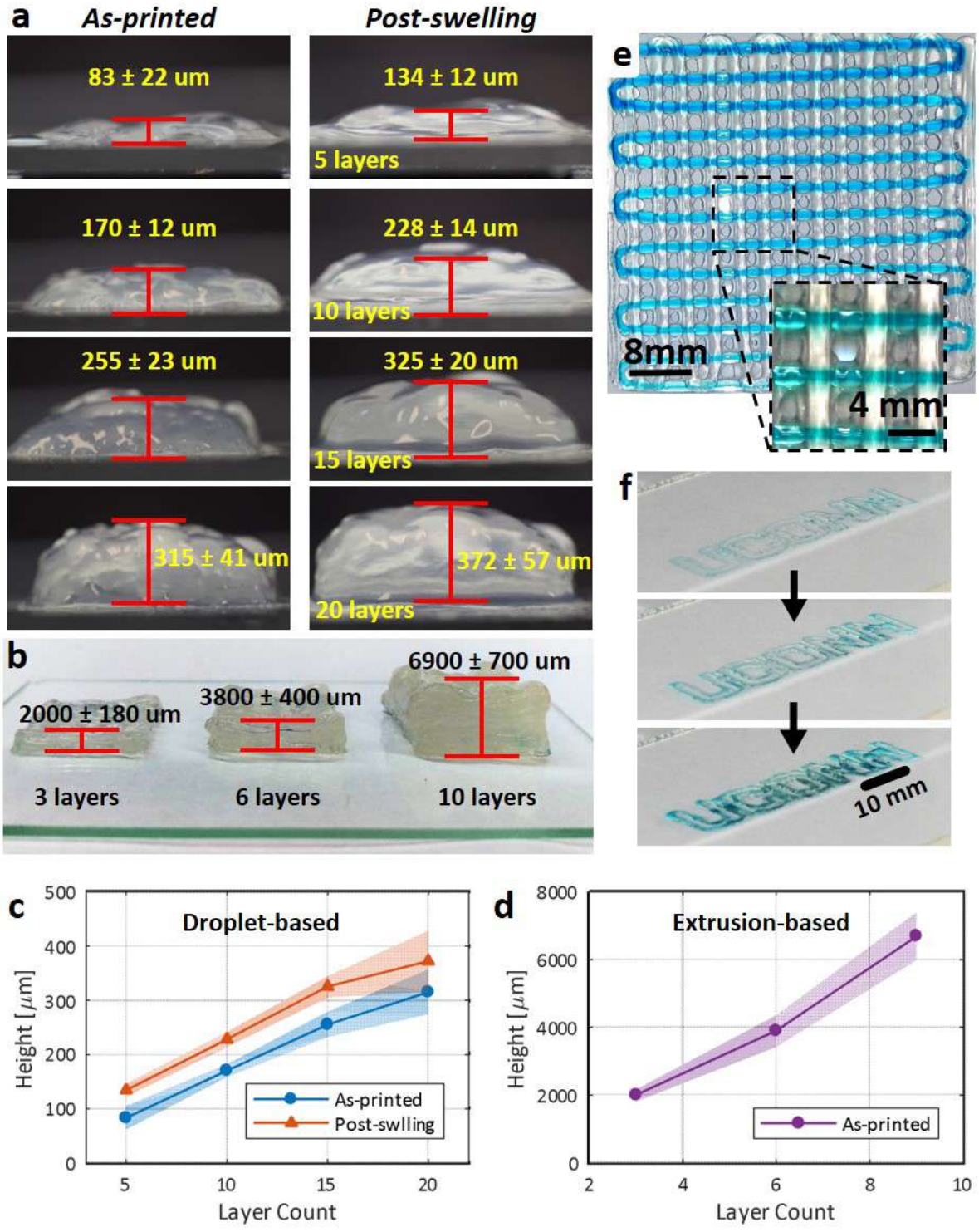

Figure 1.5. *Images of multi-layered* ***(a)*** *inkjet and* ***(b)*** *extrusion prints.* ***(c)*** *Layers vs. total height in the multi-layer prints shown in (a) immediately after printing and after swelling in PBS.* ***(d)*** *Layers vs. total height in the extruded multi-layer prints.* ***(e)*** *Two-layer extrusion print where the second layer is printed perpendicular to the first and dyed blue for better visualization.* ***(f)*** *Multi-layer inkjet print of the "UConn" logo, demonstrating a complex-design 3D print.*

Cost analysis

In addition to the unique capabilities of the proposed design, it is relatively inexpensive compared to commercial bioprinters, totaling approximately $1370. As a point of comparison, two bioprinter companies to consider are labelled here as company A and B, due to the imposed confidentiality on the given quotes. Company A offers four 3D bioprinters with one, two, three, and six pneumatic extruders, with increasing precision as the number of extruders increases, each costing $8,750, $15,250, $26,500, and $50,250, respectively. Even the most affordable of these extrusion-only printers costs over 6-fold the cost of our developed bioprinter. A 3D Bioprinter by company B, which has two separate pneumatic-based extruders, costs $11,840. A more robust, triple-extruder 3D Bioprinter by the same company, which features swappable print heads, totals to $29,140 after factoring in the cost of the swappable print heads for printing thermo-plastics, syringe-based printing, cooled pneumatic printing, and inkjet printing, and additional head for an HD camera. These commercially-available bioprinters are also 8- and 21-fold the cost of our developed bioprinter.

Approximately 36% of the total cost of the proposed bioprinter was from the mechanical components and another 36% was for the two different print heads. The custom syringe pumps account for 11% of the cost. The remaining 17% was for the electrical components of the device (Table 1.1). It should be noted that to simplify the build process of our bioprinter, we purchased readily available components, which included a single CNC unit

with its carving head included, despite the fact that we removed the head and replaced it with our custom bioprinter heads. In nearly any case, buying a complete single unit will be costlier than a bulk purchase of just the needed component(s). For instance, a bulk purchase of multiple CNC frames without the associated head can reduce the cost of our bioprinter.

Table 1. 1 Cost breakdown of the custom-developed printer

Subheading	**Total price**
Mechanical parts	$ 493
Electronics	$ 232
Printing heads	$ 495
Syringe pumps	$ 150
Total	**$ 1370**

Conclusion

By leveraging the capabilities of various modes of 3D printing and the biocompatibility of different hydrogels, we have developed a low-cost hybrid droplet-and-extrusion-based bioprinter to address the increasing demand for readily available biomimetic tissues and organs. This bioprinter is capable of direct-write bioprinting of hydrogel material in multiple layers balancing both high-resolution (using the inkjet head and photo-crosslinking) and high-throughput (using the extrusion head and chemical-crosslinking). We characterized the effectiveness of both modes of printing in various 2D and 3D custom designs and structures. To validate this approach for tissue engineering, we characterized the cell viability of mouse fibroblast cells over time. Future work will aim to integrate the two printing modes together and to characterize the viability of larger prints by using the hollow channels in the alginate to distribute oxygen and nutrients into the bulk of the printed

tissues, where diffusion is insufficient, and evaluate the homogeneity of cell-laden prints comprising multiple hydrogels. Furthermore, our platform can be benchmarked for other hydrogels and polymers, in addition to the GelMA and alginate reported, by adjusting the printer settings and parameters, such as the rate of extrusion and the droplet dispensing timing and pressure.

2. CHAPTER 2: Shape Fidelity Evaluation of Alginate Based Hydrogels through Extrusion-Base Bioprinting

Introduction

The three-dimensional (3D) bioprinting technology mainly aimed to deposit the cell-laden bioink in a predefined structure pattern with several bioprinting techniques such as laser-assisted bioprinting[57], inkjet-based bioprinting[58], stereolithography[59], acoustic encapsulation[60], valve-based bioprinting[61], and extrusion-based bioprinting (EBB)[62]. Among these techniques, EBB technique is one of the most extensively used, attracting considerable attention due to its ease of operation and high resolution printability, providing relatively sensitive 3D tissue structure[62,63,64]. There are several different variations falling under the EBB umbrella in literature, including pneumatic micro-extrusion[65] (piston-driven) and mechanical micro-extrusion[66] (screw-driven). One of the main advantages of EBB is that it has the potential for multiple print heads, providing the ability to print a range of materials and cell types, and even build cell-laden scaffolds[63,67]. EEB suffers from limitations as well, inducing large shear stress on the cell during deposition, and decreasing cell viability[68,69]. Another limitation of EBB is during deposition, the bioink is prone to deformation, which could cause the collapse of an overhanging filament. This limits the usefulness of EBB in multi-layer printing[70]. Printing low viscosity bioink with extrusion-based bioprinter limits the shape fidelity as the filament spreads post deposition, not retaining the intended shape[71].

An important step in developing a new bioink is to assess shape fidelity and printability. The printability refers to the ability of a material to be deposited in a predesigned patter with an acceptable shape fidelity, and how the printed patter matches with its CAD design[69,70]. The shape fidelity can be defined as the shape preservation of a single filament after deposition and a print accuracy when compared the printed structure to its

original design. This assessment is a major task to optimize the functionality of bioprinting and is required to estimate printing accuracy with respect to printing techniques, bioprinter type, and bioink material. There are numerous studies that assess the shape fidelity[72], extrudability[73], filament formation[74] and rheological characterization[72,75,76]. Several numerical models have been developed to estimate the optimal printing condition[77], shear thinning behavior[78], and flow behavior of bioink[79] with regards to the shape fidelity and printability.

There are several key points to take into consideration for shape fidelity with EBB. To achieve the accurate shape fidelity and control the fidelity of scaffold, the bioink needs to be selected carefully. The bioink needs shear thinning behavior, viscosity decreases with increased shear rate[80]. Ideally, bioinks should be sufficiently low viscosity to allow to the deposition, while the viscosity should be high enough to retain the desired pattern after extrusion of the bioink. The bioprinted structure needs to maintain its shape over time after remaining in a culture environment as well. Cell viability of the bioink is another one of the most important points that must be considered. High viscosity bioinks have a higher shear force during printing, decreasing cell viability[81]. Naturel hydrogels, including alginate[17], gelatin[82,83], collagen[84], and chitosan[85] have been commonly used for bioprinting due to their similarities to native extracellular matrix (ECM). However, the mechanical properties of these natural bioink components are generally poor in terms of printability. This limitation can be mitigated by adjusting the material's properties though additive materials[15,86].

Herein, we quantitatively perform two approaches assessing the printability and shape fidelity of alginate based bioink. First, we evaluate the filament collapse to estimate the

filament deformation when printing over supports of varied spacing, temperature, and alginate concentration. We develop a theoretical model to predict the Young's modulus of the filament as a function of its radius. Finite element analysis was performed to validate the theoretical model. Alginate's poor printability was then improved by adding varied concentrations of gelatin. 2-layer and 6-layer grid patterns were printed with alginate-gelatin blends, and pore area between the grid patterns was measured after printing, crosslinking and 2 day incubating at 37 °C in order to determine best shape fidelity, and effect of incubation on shape fidelity. We also tested the biocompatibility of these proposed bioink blends with cell viability test.

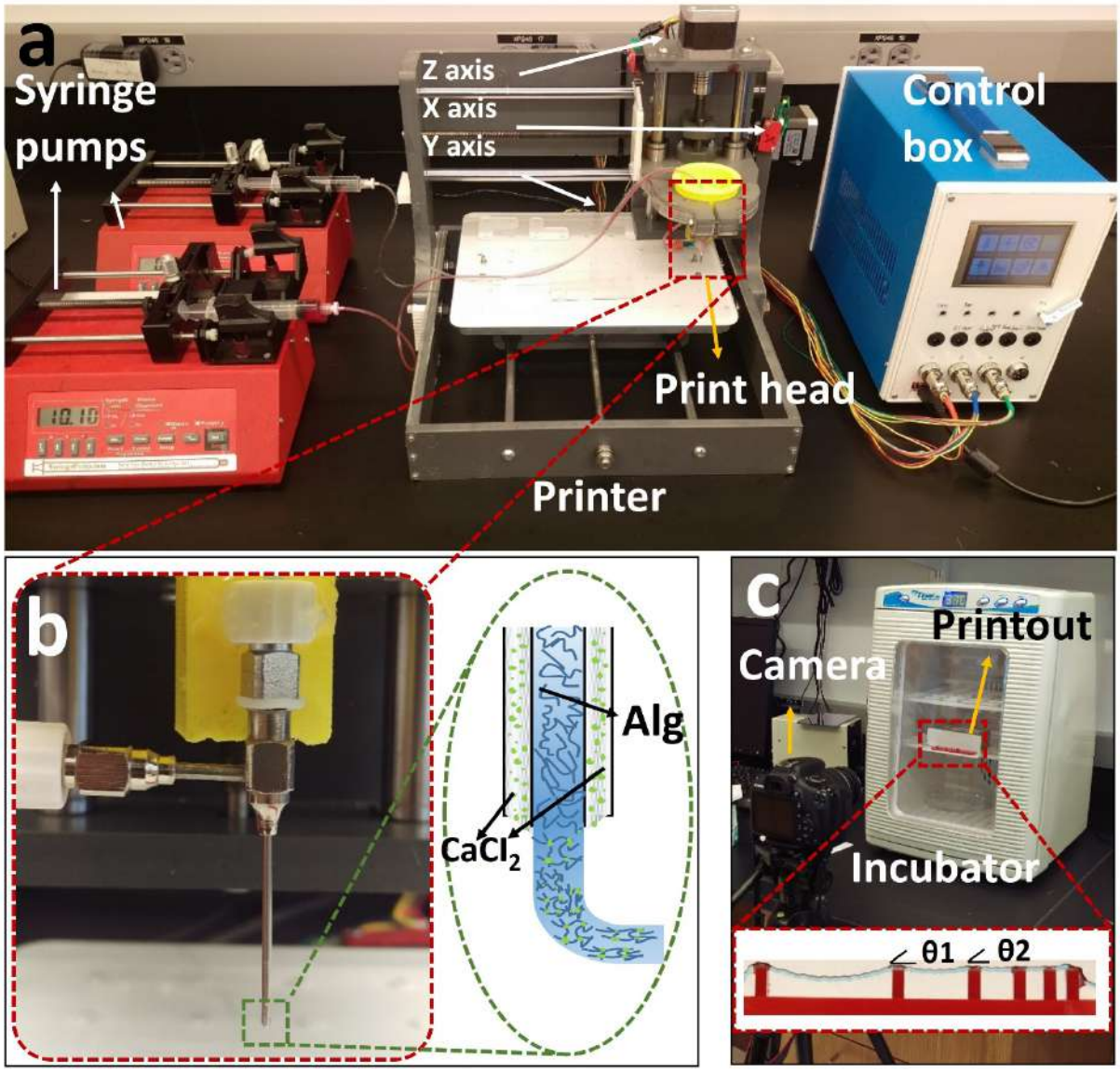

Figure 2.1. Overview of a custom-design experimental setup. (a) *Left to right: two commercial syringe pumps to extrude the hydrogel and cross-linker, custom-made bioprinter using a CNC stage as a platform, custom-made controller unit controlled via PC.* ***(b)*** *Coaxial needle and schematic illustration of printing process: cell-alginate blend and crosslinker $CaCl_2$ deposited from inner and outer needle, respectively.* ***(c)*** *Mini digital incubator with camera to image the filament deformation.*

Material and Methods

Hydrogel preparation

Alginate bio-ink was prepared as described previously[87]. In summary, sodium alginate powder (Sigma-Aldrich, US) was dissolved in phosphate buffered saline (PBS 1X, pH 7.4)

at concentrations of 2%, 4%, 6%, and 8% (w/v). Alginate-Gelatin (Alg-Gel) bio-inks were prepared by dissolving varied concentration of gelatin powder (1%, 2%, and 3% w/v) with 4% w/v alginate powder in PBS. 4% alginate concentration for the blend was selected due to its cell viability results from the previous work[87]. The bioinks were vortexed (Cole-Parmer, CT, USA) for one minute at 3400 rpm, then maintained at 37°C for one day to fully dissolve the powder(s). Red food dye was added to the bioink mixture and vortexed for 30 second to provide increased contrast. The bioink was vortexed a third time for 1 minute before loading into the syringe barrel, then incubated for 30-60 minutes at 37°C to give any air bubbles time to escape. Bioinks were crosslinked in calcium chloride ($CaCl_2$) (Sigma-Aldrich, US). This ionic cross-linker was dissolved in PBS at a concentration of 2% (w/v) by vortexing for one minute then loading it into syringe barrel.

Setup and printing parameters

We used our custom-design 3D bioprinter to perform the experiments, developed previously (Fig. 2.1a)[87]. Briefly, the bioprinter was made from a gantry-type three-axis CNC stage controlled by open-source Marlin firmware. A custom-design head holder used to hold a coaxial syringe tip (Rame-hart Instrument Co., NJ, US), with a 22G inner tip and 18G outer tip. To deposit the bio-ink and cross-linker, two NE-4000 syringe pumps (New Era Pump Systems, NY, US) were connected to the coaxial syringe tip with a silicone tubing. The syringe barrels were prepared as previously described with alginate and a 2% w/v calcium chloride solution then connected to the inner tip and the outer tip by setting the flow rate to 0.04 and 0.01 ml/m, respectively, with a nozzle speed of 4 mm/s. The system was prepared so that the calcium solution surrounds the alginate during extrusion to begin crosslinking (Fig. 2.1b).

For the pore area analysis section, we chose pneumatic extrusion (KLT-982A Auto Dispenser, Taiwan) as it has less noise at lower flow rates when compared with using a syringe pump. Syringe pumps also suffer from pressure buildup, so flow continues a short time after the pump stops. This causes additional deformity in the pattern. 30G nozzle tip was chosen to achieve high precise pattern instead of the coaxial nozzle. The nozzle speed and air pressure were set 6 mm/s and 15 psi, respectively.

Filament deformation test

The filament deformation test is based on previous works to assess the mid-point deflection of a hanged filament[88,70]. A custom platform with pillars of 1.6 x 2.75 x 4 mm (length, width, and height) placed at 1, 2, 4, 8, and 16 mm along the platform was designed in SolidWorks (Dassault Systèmes SolidWorks Corp., Waltham, MA). The design was cut with a commercially available laser cutter (VLS2.30 CO2 laser cutter; Universal Laser Systems, Inc., Scottsdale, AZ, USA) from an acrylic sheet (McMaster-Carr, Princeton, NJ, USA). Over the platform a single filament made with alginate (2%, 4%, 6%, 8% w/v) was deposited with the coaxial tip, while the process was recorded until the filament straightened horizontally due to evaporation via a Canon DSLR camera. 2D G-code was created manually in Repetier-Host (version 1.6.2, Hot-World GmbH & Co. KG, Willich, Germany), which is a free license 3D printer control software. To determine the effect of temperature on deformation, experiment was repeated in an incubator (H220-H, Benchmark Scientific, CA, USA) at temperature of 37 °C. The platform was placed in to incubator immediately after printing. Images were then taken through the incubator's transparent lid, focused on middle point of platform as seen in Fig. 2.1c. Deformation angles θ_1 and θ_2, and diameter of filament (seen Fig. 2.1c) were measured via ImageJ.

Three replicates were performed for each alginate concentration in both room temperature (25 °C) and 37 °C.

Mathematical model for filament deformation

We created a model to correlate filament deformation with Young's modules and filament radius. This model can be used to predict filament deformation. The following assumptions were made: no deformation from gravity force 20 seconds after printing, cross-section area of filament remained constant, filament density remained constant, and no outside vibrations. The Euler-Bernoulli simply supported beam equation was used to describe the shape of the filament. The general governing differential equation is as follows:

$$\frac{\partial^4 w}{\partial x^4} = \frac{P}{EI}\frac{\partial^2 w}{\partial x^2} + \frac{\rho A}{EI}\frac{\partial^2 w}{\partial t^2} = \frac{q(x)}{EI} \tag{1}$$

Where $w(x,t)$ is the displacement of filament from the neutral axis as a function of position along the filament, x and time,t. P is transfers loading that caused by adjacent beam. E is the Young's modulus, I is the moment of inertia for cylinder $I = {\pi r^4}/{4}$, ρ is the density of bio-ink (~1026 kg/m^3 for 4% alginate), A is cross-section area, $q(x)$ is transverse distributed load (force due to gravity).

Separating the displacement function $w(x,t) = e^{i\omega t}$, equation (1) becomes:

$$\left(\frac{\partial^4 w}{\partial x^4} - \frac{P}{EI}\frac{\partial^2 w}{\partial x^2} + \frac{\rho A\omega}{EI}w\right)e^{i\omega t} = \frac{q(x)}{EI} \tag{2}$$

Where ω is oscillation coefficient. We assume oscillation in the model, so $\omega = 0$. Equation (2) then reduces to:

$$\frac{\partial^4 w}{\partial x^4} - \frac{P}{EI}\frac{\partial^2 w}{\partial x^2} = \frac{q(x)}{EI} \tag{3}$$

Equation (3) is divided into two solutions:

$$\frac{\partial^4 w}{\partial x^4} - \frac{P}{EI}\frac{\partial^2 w}{\partial x^2} = 0 \tag{4}$$

$$\frac{\partial^4 w}{\partial x^4} - \frac{P}{EI}\frac{\partial^2 w}{\partial x^2} = \frac{q(x)}{EI} \tag{5}$$

Where (4) is homogenous, and (5) particular. For the homogenous solution we take ${\partial w}/{\partial x} = \lambda$ and $w = e^{\lambda x}$, equation (4) becomes:

$$w(x) = c_1 + c_2 x + c_3 e^{\sqrt{\frac{Px}{EI}}} + c_4 e^{-\sqrt{\frac{Px}{EI}}} \tag{6}$$

For equation (5), the general solution is a forth order ordinary differential equation is $w = ax^2$. Solving this equation, we get:

$$w(x) = -\frac{q}{2P}x^2 \tag{7}$$

Combining the homogenous solution (Eq. 6) and particular solution (Eq. 7), the final displacement equation becomes:

$$w(x) = c_1 + c_2 x + c_3 e^{\sqrt{\frac{Px}{EI}}} + c_4 e^{-\sqrt{\frac{Px}{EI}}} - \frac{q}{2P}x^2 \tag{8}$$

This gives us maximum deflection at $x = L/2$, the middle point of the filament. Using boundary conditions $w(0) = w(L) = 0$ and $w"(0) = w"(L) = 0$ for simply-supported beam (Fig. 2.4a), coefficients were found for each time period.

Bioink rheology

Rheological characterization experiments for alginate-gelatin bioinks were performed on a rotational AR-G2 rheometer (TA Instrument, USA) with a 40 mm in diameter and 2° cone palate and a gap with of 150 μm. Plate temperature was kept constant at 25 °C (room temperature). Shear rate was varied from 0.01 to 100 s^{-1}. The linear viscoelastic region (LVR) was determined using 0.1% strain with dynamic strain sweep. Oscillatory measurements of storage (G') and loss (G") modulus were conducted as a function of angular frequency ranging from 0 to 100 rad/s.

Compression testing was performed using dynamic mechanical analyzer (DMA, TA Q800 TA Instrument, USA). The ramp force was set at 1 N/mm to 18 N at 25 °C. Samples (10 x 10 mm and 2 mm in height) prepared as described above were placed on uniaxial parallel plate with a diameter of 15 mm. The compressive modules were calculated from the linear region of stress-strain curve. Three replicates were performed for each time point. Error bar represents the standard deviation.

Characterization of pore area

One of the main 3D printing methods is depositing the ink in a form of grid pattern with layer-by-layer manner. Likewise, main printing method, particularly for extrusion base bioprinting, is same depositing grid pattern layer by layer. Alginate concentration was set at 4% w/v for blending with gelatin to improve the alginate's printability. Gelatin concentrations were varied, using 1, 2, and 3% w/v to determine the effect of viscosity on structural fidelity. 3% gelatin is the upper limit for chosen alginate concentration as a higher viscosity would not print using the aforementioned tip size and air pressure. Pore size analysis measures the successfully printed patterns and the area within the printed

square grid pattern to determine the effect of crosslinking and incubation for multiple layers. A square grid pattern (20 x 20 mm with 11 x 11 = 121 pores) was printed in a glass slide (30 x 30 mm). Then, it was submerged in 2% calcium bath for two minutes for crosslinking. The cross-linked prints were submerged in cell culture media at 37 °C for two days. The prints were stained red dye for better imaging after printing, crosslinking and incubation, and then imaged. The images were then analyzed via ImageJ to measure the pore area.

Cell printing procedure

The procedure was conducted as mentioned above, with some changes noted here. Bioinks were prepared in sterile conditions, with. $2x10^6$ NIH/3T3 mouse fibroblast cells mixed with the bioinks immediately prior to printing. The bioink-cell mixture was deposited in a one-layer pattern. After printing, samples were immediately transferred into a well plate and allowed to crosslink for 2 min in a 2% w/v $CaCl_2$ solution. After removing the calcium solution, warm PBS at 37 °C was applied immediately followed by two washes with cell media and the samples were finally incubated for one week in cell media.

Viability characterization

Calcein AM (live green stain) and ethidium homodimer-1 (EthD, dead red stain) were used (Life Technologies) to determine the cell viability. Stained cells were observed under a fluorescence microscope (Zeiss AXIO). The samples were washed first with PBS and then a solution of 1:2000 calcein and 1:500 ethidium homodimer in PBS was applied. Each sample was submerged with the staining solution and incubated for 15 min. Images were taken over a z-axis range of 100 μm with six different focal planes spaced evenly across the z range. Cell viability was quantified by combining the six images a z-stack.

The maximum value of each (x,y) pixel across all six planes was calculated and used to create a z-projection image for each channel. The “find maxima” function in ImageJ was used for each separate channel and z position within the stack. Noise tolerance was set to 20, each local maximum in the green-channels (calcein) were taken as a live cell and red-channels (EthD) were taken as a dead cell. Viability in each image was calculated as:

$$\frac{(live\ cells)}{(live + dead\ cells)} \tag{9}$$

The mean viability for each crosslinking time was taken as the total number of live cells divided by the total number of cells (live and dead) counted across several images from two different prints. The composite images shown are pseudo-colored to show both calcein and EthD staining in a single image.

Results and Discussion

Filament deformation test

Filament deformation testing was conducted using the alginate only bioinks. Samples were prepared as described above with varying pillar distance in the deposition platform. Once deposited and crosslinked samples were left at two different temperatures for imaging to determine the deformation. Fig. 2.2a is a comparison of two deflection angles on the 4% alginate filament (at 25 and 37 °C) -. No deflection was observed in gap lengths below 4 mm. Temperature affects both *θ1* and *θ2* deflection angles are obviously seen. At 37 °C, only 6 minutes was needed for the *θ1* angle to drop to 0°, while it took 14 min at 25°C. Similarly, time for *θ2* to drop to 0° was around 9 min at 25°C, while it only took 5 min at 37 °C. This is because of the increased evaporation rate due to both the elevated temperature and decreased relative humidity. As the filament diameter is directly related

to the water content (Fig. 2.2b), temperature *de facto* effects the diameter of filament as well. It is worth noting that the diameter still decreases after the deflection angles reaches zero. The deformation on the filament due to the gravity reaches the equilibrium point with the force against the deformation caused by Young's modulus of filament.

Fig. 2.2c shows the total time where the deflection angle reaches to zero for both *θ1* and *θ2* deflection angle in room (25°C) and incubator temperature (37°C) for the four different alginate concentrations. The deflection angles are also dependent on the temperature across alginate concentrations, as can be seen in the Fig. 2.2a. Varying alginate concentrations slightly effect the total time which are around 20% in room temperature and 12% in incubator temperature for both angles. Fig. 2.2d is the positive values of slopes correlating with the diameter versus timeline as seen in b for both room and incubator temperature for the all-alginate concentrations. These results also showed that temperature effect on the diameter is seen in different alginate concentrations. The change of diameter in incubator has bigger slope than in room temperature for all concentrations. It indicates that diameter in incubator decreases faster than the diameter in room temperature due to fast evaporation as explained above. Representative images of printed filament with 4% alginate in the incubator are shown in Fig. 2.2e. It shows the deflection and diameter changing over ten minutes.

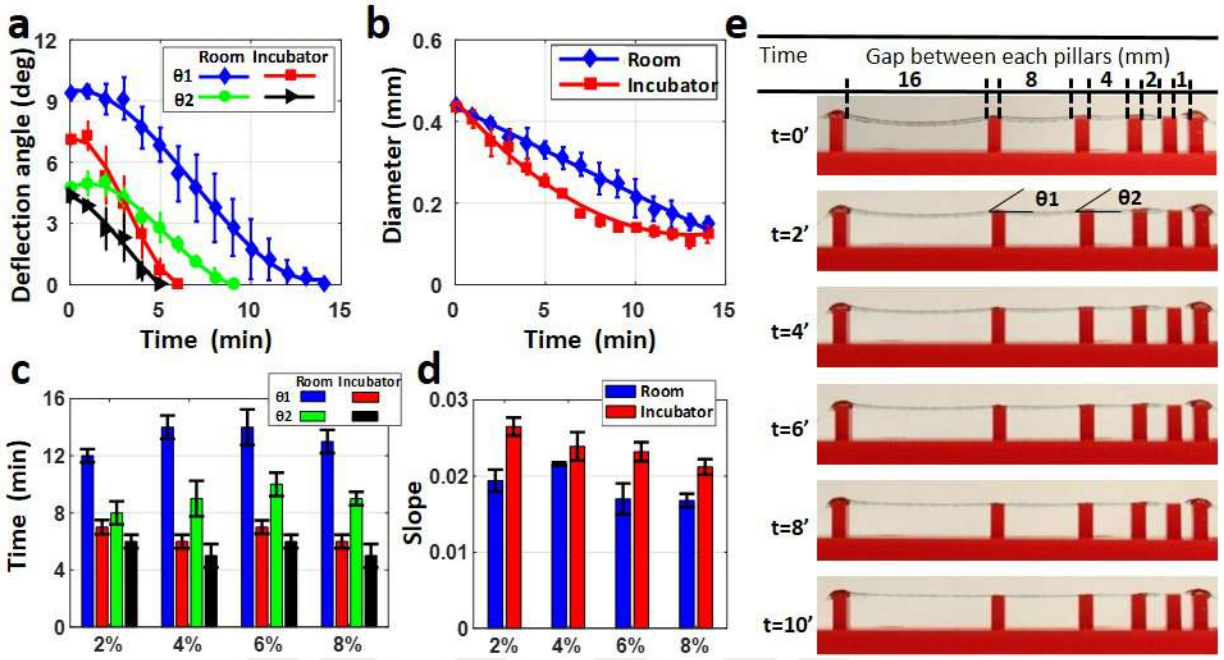

***Figure 2.2. Characterization of filament deformation in room and incubator temperatures**. **(a)** A comparison of two deflection angles on the filament in room and incubator temperatures (37 °C) over time till it becomes straight for 4% alginate (w/v) concentration. **(b)** A comparison on filament diameter changing in room and incubator temperature over time for 4% alginate (w/v) concentration. **(c)** Total time where the deflection angle reaches to zero for both θ1 and θ2 deflection angle in room and incubator temperature for four different alginate concentrations. **(d)** Positive values of slopes correlating with the diameter verses timeline as seen in b for both room and incubator temperature for four different alginate concentrations. **(e)** Representative images of printed filament over platform in incubator temperature for 4% alginate. It shows the deflection and diameter changing over ten minutes.*

Theoretical model and Finite element modeling of filament deformation

Results of the model for 4% alginate at 37 °C can be found in Fig. 2.3b. The Young's modulus of material increases as the filament radius decreases. As evaporation occurs from the filament, the ratio of solid to liquid increases, increasing the Young's modulus value. The dotted line represents the linear regression, giving the correlation between the Young's modulus and filament radius (R^2 = 0.99), which assess the elasticity modulus of filament in the condition of the known radius. Finite Element Analysis (FEA) modeling was performed using displacement magnitude for varying radius, seen in Fig. 2.3c. FEA replicates the experimental result by using data from the model. When we applied the

model's data in the FEA, we obtained the displacements shown in the legend bar next to each of the images, which is pretty consistent with the experimental results.

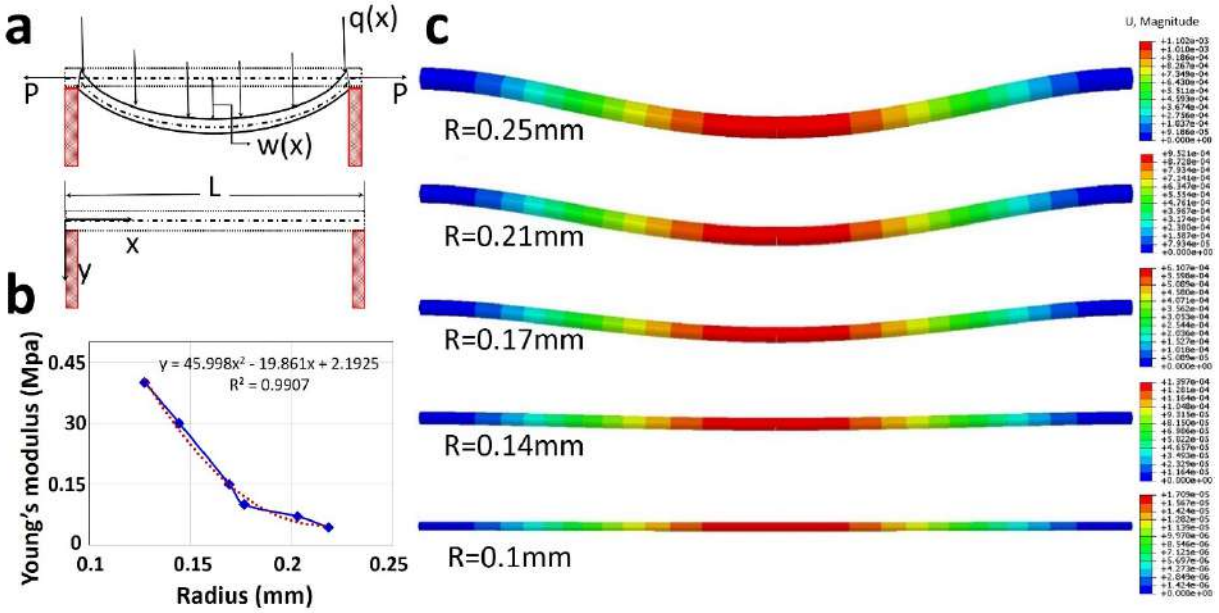

Figure 2.3. Mathematical modeling and finite element analysis (FEA). ***(a)*** *Schematic diagram of filament deformation experiment. When the filament is deposited over the two-supporting pillar, maximum deformation observed at the midpoint due to gravity. W(x) is the max displacement of filament at the middle of filament. P is transfers loading of the filament that caused because of adjacent filament,* $q(x)$ *is transverse distributed load, which is gravity force in our model.* ***(b)*** *Results of theoretical model by using the experimental data of incubation condition. It is a correlation of Young's modules and radius of filament.* ***(c)*** *Results of FEA shows the displacement on the filament due to gravity over time at which diameter of filament decreased because of evaporation. Data from mathematical model was used in the modeling. FEA was performed in Abaqus.*

Rheological characterization

Fig. 2.4a depicts the viscosity measurement results for pure alginate (0% gelatin) and its blend with three different gelatin concentrations as a function of shear rate. The viscosity curve for pure alginate vs. shear rate is relatively flat, implying that it is not suitable for bioprinting given the requirements we set out. Adding 1% or 2% w/v gelatin increased the viscosity of the bioink, but not enough to retain shape post-extrusion. Adding 3% gelatin, however, showed promising viscosity not only for printability but also preserving its shape

after deposition. The results of storage modulus, G', and loss modulus, G" of bioinks were depicted in Fig. 2.4b. The loss modulus of 0, 1, and 2% gelatin were higher than their storage modulus all over the angular frequency range of 0-100 rad/s, which indicate that these bioinks are liquid-like, cannot protect its shape after printing. However, 3% gelatin has higher storage modulus than its loss modulus, which results in a solid-like material which can retain its shape when it is deposited. Results of compression test were shown in Fig. 2.4c for all bioinks. Compressive modulus increases linearly with increasing gelatin concentration from 0.5 to 1.8 kPa for the 0 and 3% gelatin, respectively. As a result, the rheological and mechanical features of bioink made with pure alginate is insufficient for the bioprinting due to its low viscosity and compressive modulus. Those properties were easily improved to be able to reach high shape fidelity by the addition of gelatin. 3% gelatin in 4% alginate showed ideal rheology and mechanical strength, and it has good potential for further bioprinting.

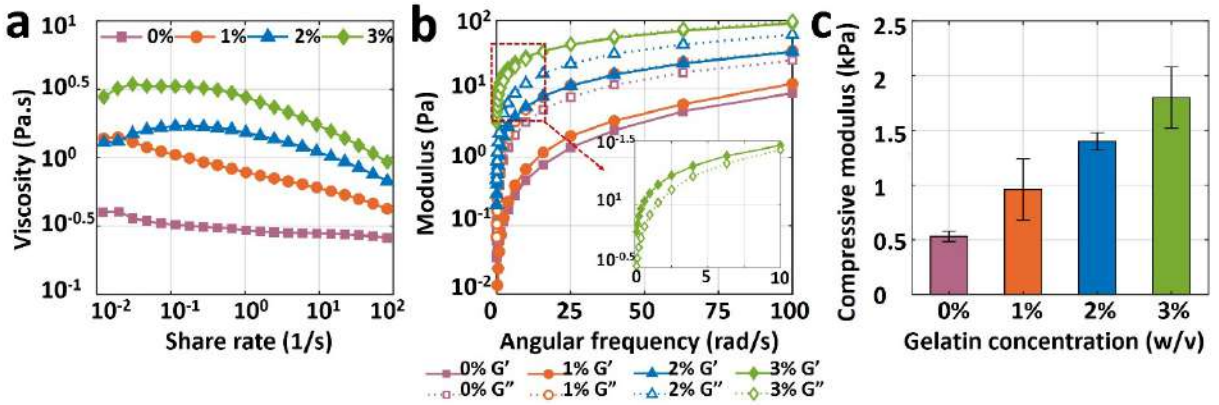

Figure 2.4. Results of rheological and mechanical characterization of bioinks. (a) *Viscosities of 4% pure alginate (0%) and the addiction of 1%, 2%, and 3% gelatin in alginate as a function of shear rate ranging from 0.01 to 100s^{-1}.* ***(b)*** *Storage modulus (G') and loss modulus (G") of all bioinks as a function of angular frequency ranging from 0 to 100 rad/s.* ***(c)*** *Compressive modulus of 3D bioprinted and crosslinked samples with four different bioinks. A square of 10 mm wide and 2 mm thickness sample was placed on platform of DMA and compression was preformed until samples was yield. Error bar is the standard deviation of 3 repetitions.*

Pore area analysis

Representative images and quantitative results of pore area measurement analysis depicted in Fig. 2.5. The representative images of 6-layer printed pattern with four different bioink mixtures are shown in Fig. 2.5a. First column is the images that were taken after printing and second column is for after 2 days' incubation. From Fig 2.5a, the 4% pure alginate filled in the pore area after deposition due its low viscosity, which cannot keep its shape and spread around easily. The print quality improved with 1% w/v gelatin added compared with pure 4% w/v alginate, and continues improving with increasing gelatin content through 3% w/v. Past 3% w/v gelatin, the high viscosity of the bioink precluded printing. The quantification of experimental images is presented in Fig. 2.5b-e. Fig. 2.5b and c show normalized pore number – percentage of successfully printed pores of 2-layer print and 6-layer print, respectively, for after printing (1), after crosslinking (2) and after incubating for 48 hours (3). In 2-layer samples: 0% gelatin maintains around 25% normalized pore number after printing, after crosslinking and after incubating. Increasing to 1% w/v gelation in alginate increases to 50% normalized pore number, 2% and 3% gelatin increases to 98%. This increase is due to the increased viscosity providing better printability. For the 6-layer print as seen in c, 0% gelatin would not hold a grid pattern, resulting in a normalized pore number of 0%. Comparing the 6-layer to 2-layer prints, the normalized pore number decreased approximately 70% for 1%, and 2% w/v gelatin in alginate due to filament collapse due to low bioink viscosity. However, there were no decrease observed for 3% w/v gelatin for after printing and after crosslinking other than 10% decrease for after incubation. 3% w/v gelatin in alginate once again gives the best print quality for all three conditions.

The quantification results of pore area measurement with all bioinks for 2-layer and 6-layer prints are shown in Fig. 2.5d and e, respectively. These data show crosslinking does not highly affect the pore area. However, there is a slight increase on the pore area after incubation in all bio-ink types for both layers. There was 35% increase in the pore area of 3% for 6-layer print. This increase might be caused because of that crosslinked solid print can be expanding with effect of temperature, which is increased the pore area. The error bar was obtained from successfully printed pores and the average of three reputations of each single experiment.

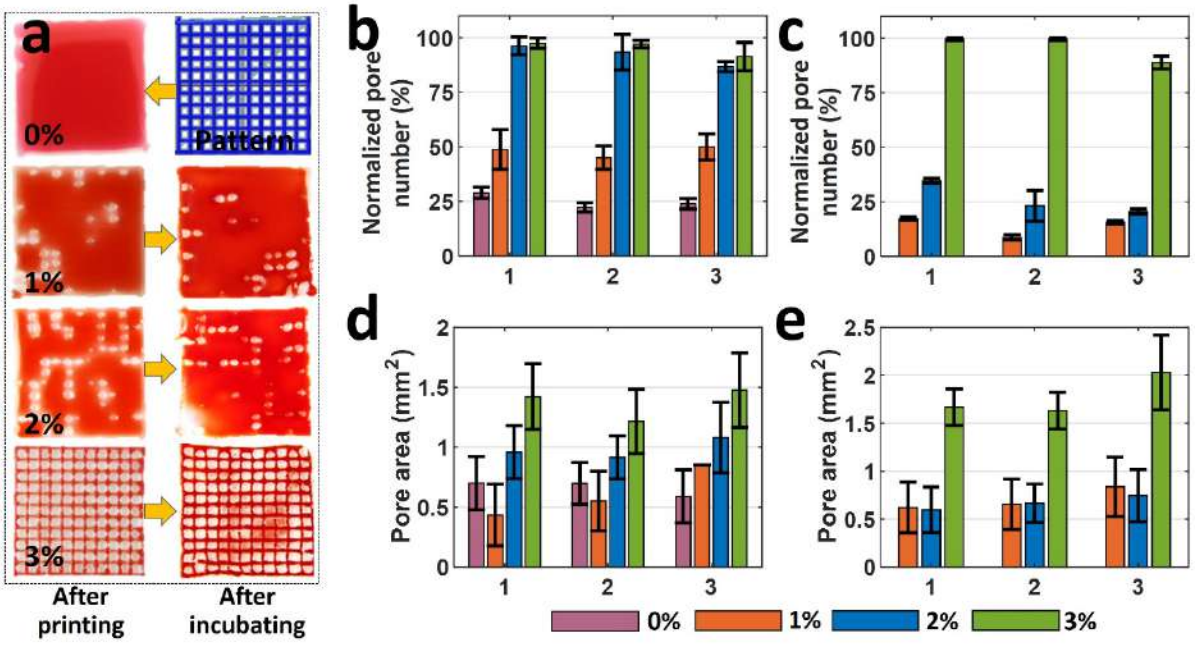

Figure 2.5. Characterization of print quality and pore area for multiple layers grid pattern. ***(a)*** *Images of 6-layer printed pattern with four different bio-ink mixtures. First column is the images that were taken after printing and second column is for after 2 days' incubation.* ***(b-c)*** *Normalized pore number that shows the percentage of successfully printed number of the pores for after printing, after crosslinking and after 2 days' incubation* ***(b)*** *for 2-layer print and* ***(c)*** *for 6-layer print.* ***(d-e)*** *Pore area measurements* ***(d)*** *2-layer print and* ***(e)*** *6-layer print after printing, after crosslinking, and after 2 days' incubation. There are no results of 0% for 6 layers due to bioink filled the whole pores in grid pattern as seen in a. (x-axis for plots are* ***1****: After printing,* ***2****: After crosslinking,* ***3****: After incubating).*

Cell viability analysis

The gelatin concentration was varied to characterize the effect of gelatin concentration in 4% alginate on the cell viability. The fluorescence images of printed NIH 3T3 mouse embryonic fibroblast cells in 4 different bioinks over 7 days are showed in Fig. 2.6a. The cell viability results for varying gelation concentration are depicted in Fig. 2.6b. Pure alginate has the lowest cell viability at 70%, adding gelatin increases cell viability by around 15% on day 0 (right after printing). We observed the highest viabilities on day 5WE over a week incubation for all bioinks. The highest cell viabilities for pure alginate showed 29% increase to 91% within 5 days incubation while the viabilities were increased 1%, 11% and 16% for the 1%, 2% and 3% gelatin, respectively when we compare day 0 and day 5. The lower increases for 1%, 2% and 3% gelatin than pure alginate could be attributed to the higher mechanical strength of them which may prohibit the nutrient and oxygen transfer to the cells. On day 7, the viabilities for all bioinks decreased ranging around 4-14% which could be attributed to the lack of nutrient and oxygen. We observed also that the highest cell viability belongs to the 3% gelatin on day 7. In conclusion, proposed bioinks, 3% gelatin, are biocompatible and have excellent potential for 3D bioprinting tissue and organ.

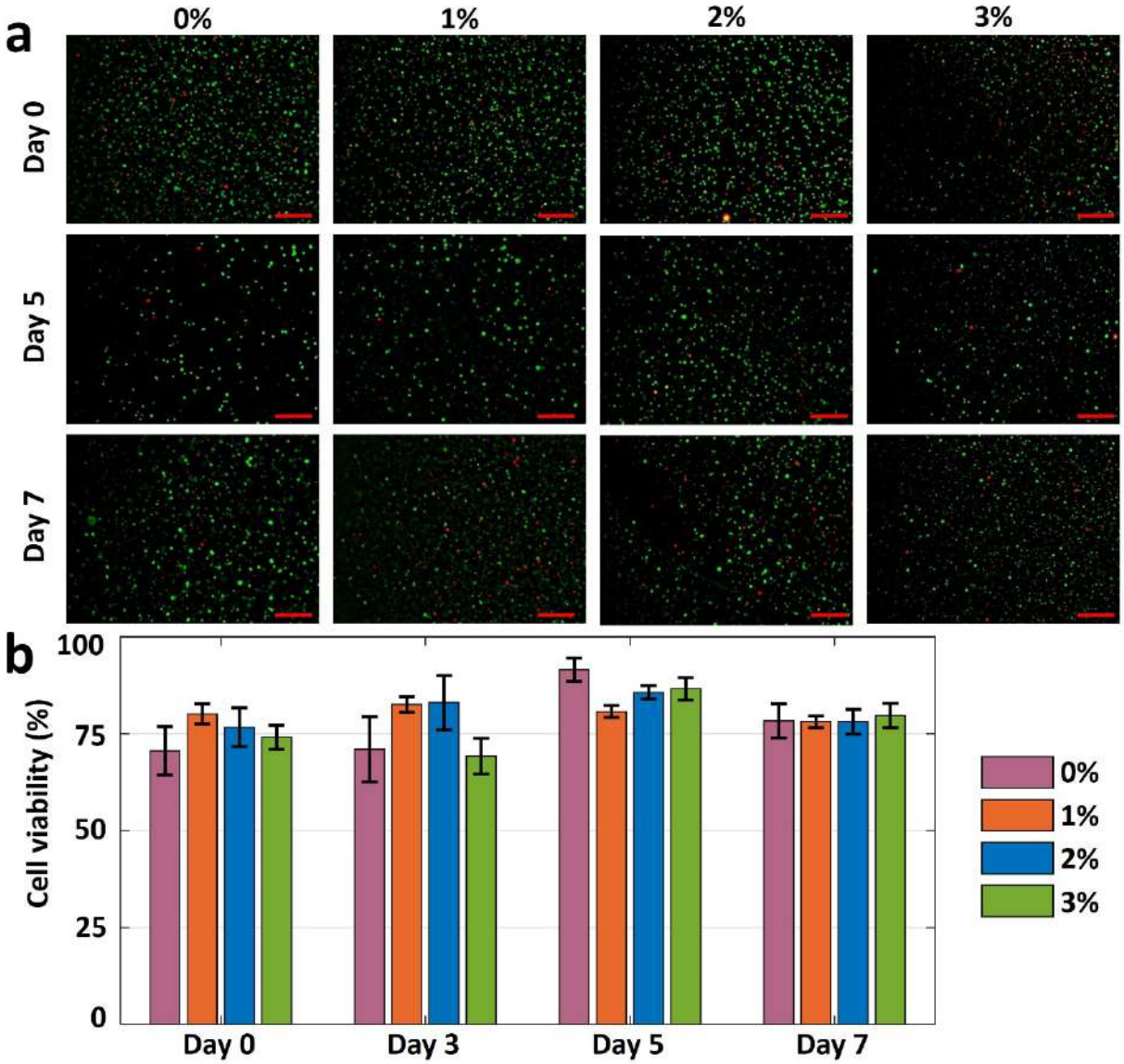

Figure 2.6. Characterization of cell viability. (a) *Fluorescence images of National Institutes of Health (NIH) 3T3 mouse embryonic fibroblast cells in four different hydrogels showing the cell viability after day 0, 5, and 7. The green stained (Calcein AM, 0.5μL/mL) cell represents the live cell. Red stained (ethidium homodimer 1, 2μL/mL) cell represents the dead cell. Scale bar represents 500 μm.* ***(b)*** *Quantification of the cell viability from live/dead image analysis. Error bars represents the standard deviation of three independent measurements.*

Conclusion

Developing multiple component bioink formulations with high shape fidelity requires qualitative fidelity analysis and prediction methods. We have demonstrated two shape fidelity analysis techniques and a mathematical model using our custom bioprinter. The shape fidelity analysis methods developed herein offer readily accessible and replicable techniques to rapidly optimize new bioink formulations. They can help accelerate the development process by evaluating the performance of new bioinks for shape fidelity. The first technique evaluates the shape fidelity based on physical deformation of a single printed filament over a platform in two temperature (25 °C and 37 °C). The results from this technique provides an idea how the bioink will behave in different temperatures. The second technique focuses on improving the printability and structural fidelity of a bioink. Evaluating bioink formulations is crucial to print more complex architectural constructs. The crosslinking and incubating process is the most delicate portion because maintaining shape fidelity directly effects to the performance. Finally, we demonstrated a method to determine the biocompatibility of proposed bioinks for use in tissue engineering. We characterized change in cell viability of NIH 3T3 mouse fibroblast cell over time. By considering the accessibility and repeatability, these proposed methods should prove highly suitable for bioink development and help accelerate the process.

3. CHAPTER 3: Fidelity analysis of biodegradable patches made with alginate-cellulose hybrid bioink

Introduction

Millions of people suffer from tissue loss or organ defects, contributing to over $400 billion per year total healthcare expenses in the United States[1]. Tissue engineering has the potential to help overcome these challenges through the development of regenerative tissues, autologous cells, biodegradable scaffolds, and various implants such as arterial reconstruction[2] and bone regeneration[3]. Multi-material and multi-functional biodegradable patch research is a promising field, it offers increased functionality, cost-efficiency, and production feasibility with organic and inorganic materials; moreover, they are biodegradable, meaning that they are gradually extinguished from the body after fulfilling their functions. Biodegradable patches have been used for a variety of reasons, including restoring function, facilitation healing, and replacing organs such as skin or tissues after injury or disease. Biodegradable patches have been used for different applications including wound healing[4], cardiac reconstruction[5], health monitoring[6], and drug delivery[7]. Their use in wound healing is particularly promising. The skin is the largest organ in the body and is an open door for potentially harmful impairments or injuries such acute trauma, burns, surgical defects, or long-term diseases such as eczema and diabetes[4,8]. A skin injury larger than 4 cm will not heal without external support[9], often requiring donor skin; however, the availability of donor skin is limited. Biodegradable patches offer a robust alternative solution via composition of non-toxic and non-allergic materials.

The first biodegradable patches were single- or multi-layered patches with no spatial heterogeneity in planar material properties or functionality[10]. Recently, with the growth of wearable technologies and their emerging applications, electronics have been integrated

into patches and spatially heterogeneous material deposition has been achieved[6,8,7]. From this perspective, 3D bioprinting can be used for the high throughput fabrication of these patches via multi-material deposition without requiring manual handling or steps. Bioprinting can readily produce custom biodegradable patches that are compatible with specific native tissues, such as external blood vessels and bone, and has potential to engineer fully functional organs as well as patient-specific tissues. Furthermore, modern applications of patches, such as health monitoring, require complex electronic integration with electronic sensors[6], which can be achieved by 3D bioprinting at high throughput, potentially in a single step. Thus, 3D bioprinting technology is expected to be increasingly used to generate patches due to its ability to deposit multiple materials in a single step. Here, we leverage these unique advantages of bioprinting technology to fabricate free-template, multilayer, and heterogeneous complex patches.

Fidelity is one of the main aspects of patches influencing their functionality. A patch must maintain its shape and structure for some time on the target tissue or organ, then biodegrade after fulfilling its role. Mechanical loading is an important design consideration; for example, patches have been proposed or developed to serve as pressure sensors on vessels[6] and organs, and as repair materials for cardiac reconstruction in patients with complex congenital heart defects[5]. In tissues that undergo periodic dilation and constriction, the shape of the patch and its material properties, biodegradability, and electronic components may be affected. It is critical to ensure that a patch maintains its fidelity under the mechanical loading over the targeted time. Depending on the target organ or vessel, patches are intended to stay in the body for various lengths of time. For instance, a patch for monitoring blood flow may stay on a

vessel for twelve weeks[6], while a cardiac patch might remain on an organ for ten weeks[11]. In addition, patches are usually prepared at room temperature (22-26 °C) before being applied to the body (37 °C). This temperature difference can affect the fidelity of a patch.

3D bioprinting technologies offer rapid and early wound treatment to avoid aggravation, tissue damages, and hypertrophic scarring for multiple types of wounds including, burn, diabetic, surgical wounds. The 3D bioprinting technologies had been stared to use for wound healing and skin regeneration in 2012 using naturel bioink collagen and it reached around 70 published studies by 2020[89]. Extrusion based bioprinting is the widely used method[90] and various crosslinking method were used such as, chemical crosslinking by calcium chloride[91], and UV light[92]. Collagen[93], gelatin[91], and alginate[94] are bioink materials used for wound healing due to their properties, such as similarity to the extracellular matrix (ECM), printability, and biocompatibility. Most of the in vitro studies employed the fibroblast skin cell such as human dermal fibroblast cell[95] and 3T3 mouse fibroblast cell[92]. In addition to the in vitro study, there are many animal studies conducted for wound healing by using mice[90,95], rats[96,97], and porcine[90].

To achieve high fidelity (performance) bioprinted cell-laden patches, one of the most important factors is the hydrogel material (bioink)[98,99,100,101,102]. The hydrogel needs to have enough viscosity to preserve its shape after deposition and must keep its shape post crosslinking. Bioprinting hydrogel has several requirements, including effective printability, biodegradability *in vivo*, and strong and elastic physical properties for mechanical loading[12]. Alginate is a widely used hydrogel material in bioprinting due to its low-coast, easy and rapid crosslinking with calcium chloride, innate biocompatibility, while maintaining high cell viability. Alginate, however, has several drawbacks to its use in

bioprinting, including low mechanical properties, low viscosity, slow degradation, and limited printability[13]. This limits its design and use in some applications that required mechanical loading, such as a cardiac implant. To counter this issue, other materials can be added to increase the viscosity and mechanical strength. For example, the structural fidelity of printing with alginate had been increased by blending the alginate with carbon nanotubes (CNT)[14], gelatin methacryloyl (GelMA), hydroxypatite[13,17], and cellulose[18,19].

Cellulose nanoparticles are one of the most attractive co-materials for tissue engineering. Cellulous nanoparticles have several advantages including sustainability, biocompatibility, abundance, water-retention, and high chemo-mechanical properties[20,21,22]. Cellulous nanoparticles can also be found in different forms, including cellulose monocrystalline (CNC) which is used for many applications including reinforcing alginate-based hydrogels[23]. Another form is cellulose nanofibril (CNF) which is used to improve rheological and mechanical properties of pure alginate with respect to printability and structural fidelity[24]. Of particular interest is one form of CNF, TEMPO-mediated oxidation cellulose nanofibril (T-CNF), which shows excellent printability, mechanical strength, and viscosity within the ideal range[25]. Even though GelMA provided higher cell viability than alginate hydrogels in our fist study[87], we chose the alginate-cellulose hydrogel due to GelMA has been already demonstrated in many studies[15,16]. Moreover, alginate-based hydrogels are more suitable than GelMA for extrusion-based bioprinting.

We characterize the concentration of CNC and CNF based hydrogels and printing parameters such as pneumatic pressure, nozzle speed, and line thickness to achieve the best shape fidelity with our custom-made bioprinter[87]. We also characterize the rheological properties of optimized hydrogels such as viscosity, and storage-loss

modulus, and performed mechanical characterization of 3D printed and crosslinked patch samples through mechanical loading. Finally, we conduct a biodegradability and biocompatibility characterization by exposing the patch in a chemical solution that mimicking the body, and bioprinting mouse fibroblast cells in both bioinks over time. This study provides a foundation to develop new patch materials with high printability, fidelity, and biocompatibility. The fidelity analysis methods presented could open a way to enhance the performance of biodegradable patches that can be implanted for wound healing.

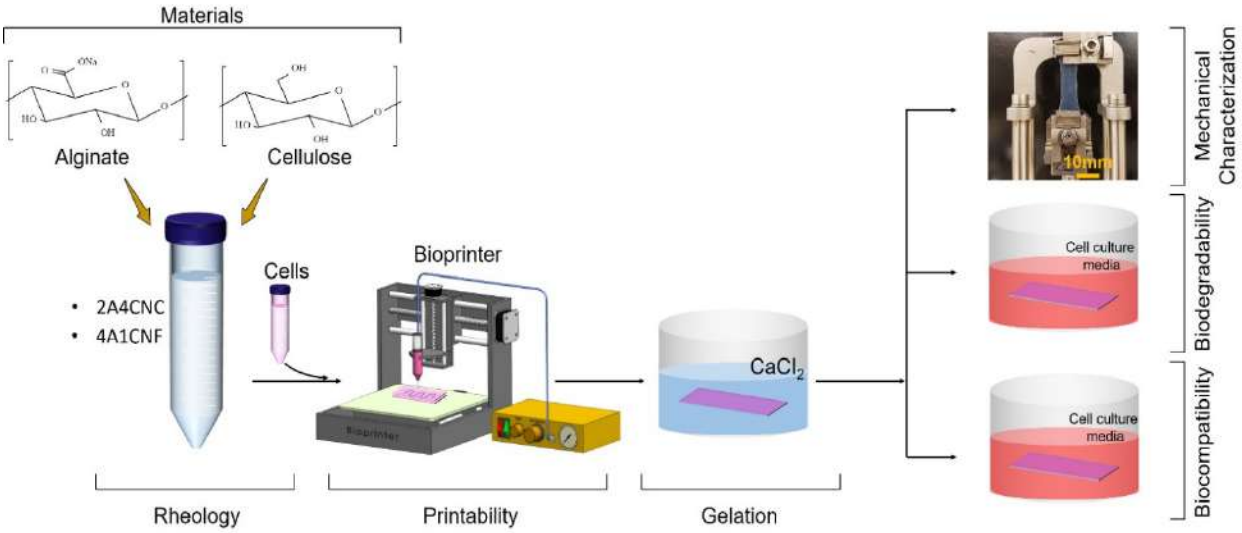

Figure 3.1. Schematic illustration of experiment process.

Material and methods

Materials

Sodium alginate powder and calcium chloride ($CaCl_2$) were acquired from Sigma-Aldrich (Missouri, US). TEMPO (Anionic type) Cellulose Nanofibrils (T-CNF) Slurry (1% w/v solid in water, Width: 20-50 nm; Length: 0.5um - 80um Surface Group: Carboxyl Hydrophilic) was obtained from Cellulose lab (New Brunswick, Canada). Cellulose Nanocrystals

(CNC) spray-dried powder hydrolyzed from wood was purchased by CelluloForce (Montréal, Canada). HyClone Dulbecco's Modified Eagle's Medium with high glucose (DMEM, GE Healthcare Bio-Sciences AB, Sweden) was purchased from cytiva (Global Life Sciences Solutions USA LLC MA, USA), Fetal Bovine Serum (FBS, Premium) was obtained from Atlanta Biologicals (GA, USA). Penicillin-Streptomycin (Gibco, for mammalian cell culture) and cell viability kit (Invitrogen) for cell viability were obtained from ThermoFisher Scientific (NY, USA).

Bioink preparation

Alginate and CNC powder were dissolved in Milli-Q DI water at concentrations of 2% and 4% (w/v) respectively and vortexing for homogeneity (Cole-Parmer, CT, USA) for 2 min at 3400 rpm. The CNC concentration was chosen as it gave best printability[103]. To prepare the Alginate-T-CNF bioink, alginate powder (4% w/v) was added into the T-CNF solution (1% w/v solid in water) and then vortexed at least 2 min at 3400 rpm. Best shape fidelity was achieved using 4% alginate and 1% T-CNF. The bioinks were maintained at 37 °C for several hours for rapid dissolving. Prepared bioinks were then loaded into 5 mL syringe barrels. The ionic crosslinker, $CaCl_2$ powder was dispersed in Milli-Q water at 2% (w/v) concentration by mixing on a vortex at 3400 rpm for 1 min. We will abbreviate Alginate-CNC as 2A4CNC and Alginate-T-CNF as 4A1CNF.

Printability and characterization of bioinks

Previously prepared syringe was placed on the printer using a custom-designed 3D printed syringe holder. A 20 x 20 mm grid pattern was designed on SolidWorks (Dassault Systems SolidWorks Corp., Waltham, MA) and saved as a STL file. The STL file was converted to the G-code as a form of 16 layers' grid pattern by a slicing engine Slic3r.

The nozzle speed was set constant to 7 mm/s for all prints. An air regulator (KLT-982A Auto Glue Dispenser, Taiwan) was used to deposit the bioink on glass slide with 30G syringe dispensing tip on the printing platform as seen in Fig. 3.1b. Different air pressures were tested to determine the best print quality: 8, 12, and 18 psi for the 2A4CNC bioink and 10, 20, and 30 psi for the 4A1CNF bioink. All samples were then cross-linked in a 0.18 M calcium chloride solution for two min. After crosslinking, samples were imaging by a Carson eFlex digital camera (Carson Optical, Inc., NY, US). To characterize the line thickness for both bioinks a one-layer grid pattern was printed and imaged. Line thickness was measured with ImageJ. Optimal air pressures were used to synthesize samples for the rest of the experiment. Different geometries were used for the different experiments: for mechanical characterization and swelling tests, a two-layer geometry (20 x 10 x 0.5 mm) was used, for compression and degradation tests an eight-layer geometry (10 x 15 x 2 mm) was used. Samples were kept in DI water until needed for characterization experiments.

Rheological characterization

The rheological properties of bioinks and their components (2% Alg, 4% CNC, 4%Alg, and 1%T-CNF) were analyzed using a rotational AR-G2 rheometer (TA Instrument, USA) with a 40 mm in diameter cone palate and a gap with of 150 μm. All measurements were done at 25 °C and samples were allowed to reach equilibrium for one-minute subsequent to adding sample to the test platform. Shear rate range was varied between 0.01 to 100 s^{-1} to measure the viscosity. Dynamic strain sweep was carried out by using same cone plate to determine the linear viscoelastic region (LVR). 1% strain sweep of strain was

selected for the test. The frequency sweep was then used to estimate the storage modulus (G') and loss modulus (G'') as a function of angular frequency of 0-100 rad/s.

Mechanical characterization

Samples were mechanically tested using a TA Q800 Dynamic Mechanical Analyzer (DMA) to find the Young's Modulus in the slope in the initial linear region of the stress-strain curve. Samples were exposed to a ramped force (stress), force ramp rate of 0.1 N/min. Simultaneously, resultant deformation (strain) was monitored until the sample failed. Maximum deformation before failure ("Elongation at break") was also determined. Cyclic loading tests were carried out to assess hysteresis (deformation in response to cycling) over time, mimicking movement in the skin. The cycle tensile was performed in DI water to avoid drying. 100 cycles were performed, strain was ramped up and down at 10%/min between 0% and 20%, mimicking the maximum strain on the skin of human wrist[104]. Hysteresis was calculated from the stress-strain curve of inside area of loading and unloading. This experiment was carried out at 25 °C.

Swelling test

3D printed samples were dried at 37 °C overnight in incubator and then weighed. The dried samples were then submerged in DI water bath in room temperature for up to 96 hours. The swelling was measured at specific times (1, 2, 4, 6, 8, 24, and 96 h) and excess surface water on the sample was removed via blotting before weighing. After measuring was completed, the samples were returned to the DI water bath. The swelling ratio was calculated for samples using the following equation[105]:

$$S = \frac{w_s - w_d}{w_d} x100 \qquad (10)$$

where, S is the percentage of swelling of the samples; w_d and w_s are the dry weight and swollen weight of the sample, respectively. The test was conducted with three different samples for each bioink, error bars reflect standard deviation.

Thermal analysis

Phase transitions were determined by differential scanning calorimetry (TA, instrument, DSC Q20), to estimate the melting temperature. Samples weighing between 4 and 10 mg were placed into hematic aluminum pans, ramped from -50 °C to 250 °C at 10 °C/min, held for 5 minutes, before being cooled to -50 °C and cycled again under nitrogen atmosphere. The first heating cycle was used for the analysis of the phase transitions of the samples. The heat flow (W/g) was reported as a function of the temperature. The melting temperature was determined as the lower peak point of curves.

Decomposition profiles of 2A4CNC and 4A1CNF bioink samples were determined by thermogravimetric analysis (TA instruments, TGA Q500), to determine the degradation temperature of the hydrogel. Samples were ramped from room temperature to 600 °C at a rate of 10 °C/min under nitrogen atmosphere. Percentage weight loss was determined as function of the temperature. Degradation temperature was set as the beginning point on each curve of TGA line[106].

In vitro degradation test

3D printed samples (10 x 15 x 2 mm) were placed in an environment meant to mimic a living body. Media containing Dulbecco's modified Eagle's medium (DMEM) with 10% fetal bovine serum (FBS) and kept at 37 °C and 5% CO_2 in an incubator, and was replaced every 2-3 days. Periodically, samples were removed from incubator, washed with distillated water, freeze-dried for three hours, weighted and then imaged. Samples were

sterilized with UV-light for 20 min before being replaced in the incubator. Normalized weight loss of the samples were calculated with the following equation[107]:

$$Normalized\ Weight\ Loss = \frac{w_i - w_f}{w_i} x100 \quad (11)$$

where, w_i is the initial weight w_f is final weight after being freeze-dried. Degradation tests were conducted three times for each bioink with error bars representing standard deviation.

Compression test was also carried out to investigate the effect of degradation on the material stiffness. Fabricated samples (10 x 10 x 2 mm) were kept in the media in the incubator (at 37 °C and 5% CO2) and removed from the media and measured every 5 days over a total span of 30 days. Once removed, samples were washed with distillated water before compression testing at room temperature. Compression tests were performed using dynamic mechanical analyzed (DMA). Force was ramped at 1 N/mm to 18 N. Prepared samples were placed on uniaxial parallel plate with a diameter of 15 mm. Compression was stopped when sample yielded. Compressive modules were calculated from the linear region of stress-strain curve. Three replicates were tested for each time point. Error bars represent standard deviation.

Bio-printing procedure

Hydrogel biocompatibility was evaluated employing NIH/3T3 mouse fibroblast cells (American Type Culture Collection, Manassas, VA, USA). Fourth stage cells were cultured according to the ATCC protocol over a week to reach the sufficient cell density. Syringes were prepared with 2A4CNC and 4A1CNF hydrogels, and sterilized by UV for 20 min. Sterile conditions were maintained, and $3x10^6$ 3T3 NIH mouse fibroblast cells

were mixed with the bioinks right before the printing. The nozzle speed was set to 7 mm/s and air pressures were set 12 psi and 20 psi for the bioinks of 2A4CNC and 4A1CNF, respectively. The bioink-cell mixture was deposited on a single layer. After printing, the samples were transferred into a well plate and $CaCl_2$ solution was applied to crosslink the bioink for two min. After removing the calcium solution, samples were submerged in warm PBS followed by two washes with cell media immediately following crosslinking. The bioink samples were kept in cell media at 37 °C up to 10 days.

Viability characterization

Cell viability characterization was based on our previous work[87]. Briefly, calcein AM (stains live cells green) and ethidium homodimer-1 (EthD, stains dead cells red) stains were used (Life Technologies). The stained cells were then imaged with a fluorescence microscopy. Samples were washed with PBS, followed by a solution of 1:2000 calcein and 1:500 ethidium homodimer in PBS. Each sample was incubated for 15 min in the staining solution. Images were captured in six different focal planes in the z-axis over a range of 100 μm. The six images were combined into a z-stack and the maximum value of each (x,y) pixel across all six planes was used to create a z-projection image for each channel separately to quantify the cell viability. From each image, the “find maxima” function in ImageJ[56] was used with a noise tolerance value of 20 to identify local maxima in the image. The local maximum in the green-channel (calcein) was taken as a live cell and each local maximum in the red-channel (EthD) image was taken as a dead cell. The cell viability of each image was calculated using:

$$Cell\ Viability = \frac{live\ cells}{live\ cells + dead\ cells} \tag{12}$$

The viability for each crosslinking time was averaged across several images from two different prints. The composite images shown are pseudo-colored to show both calcein and EthD staining in a single image (Fig. 3.6a, b).

Statistical analysis

In order to evaluate the statistical significance, one-way ANOVA tests for multiple comparison and t-test for two samples comparison were performed. Analysis was conducted with Microsoft Excel. A value of $p<0.05$ was considered to state statistical significance. All quantitate data were presented as mean ± standard deviations.

Results and discussion

Printability and shape fidelity

Assessing the printability of bioinks is important to achieve shape fidelity. Bioink components, concentrations, mechanical properties during 3D printing such as air pressure, extrusion speed, and nozzle size are all important factors. In our study, we used a formula of alginate and CNC hybrid bioink as having the best shape fidelity from literature[103]. We experimentally tested alginate-CNF bioink formula in terms of printability. We varied the extrusion pressure to find optimum at three different air pressures of 8, 12, and 18 PSI for 2A4CNC and 10, 20, and 30 PSI for 4A1CNF as seen in Fig. 3.2a. Low air pressure does not provide enough force to extrude the bioink as a desired pattern, it caused intermittent printing as seen in Fig. 3.2 a1 and b1. High air pressure causes overflow, which spreads around and fills the gaps in the grind pattern as seen in Fig. 2 a3 and b3. We determined the optimum air pressure of 12 psi and 20 psi for the bioink formulation of 2A4CNC and 4A1CNF, respectively. The print accuracy of 2A4CNC hydrogel matched with the previously reported study using the same alginate-CNC

hydrogel concentration[103]. The optimized alginate-CNF ratio hydrogel had better shape fidelity than those reported for either pure alginate or pure CNF[108].

Fig 3.2c depicts thickness of a single line as a function of extrusion air pressure, showing the effect of air pressure on filament width. Line thickness using 2A4CNC is much larger than that of 4A1CNF due to the higher viscosity of 4A1CNF. 4A1CNF was more structurally robust and retained its shape after printing compared with 2A4CNC. Fig 3.2d and e are representative images of 2-layers grid pattern after 2 min cross-linked in calcium. Those images also demonstrate that the print with 2A4CNC has dull color and print with 4A1CNF has transparent color.

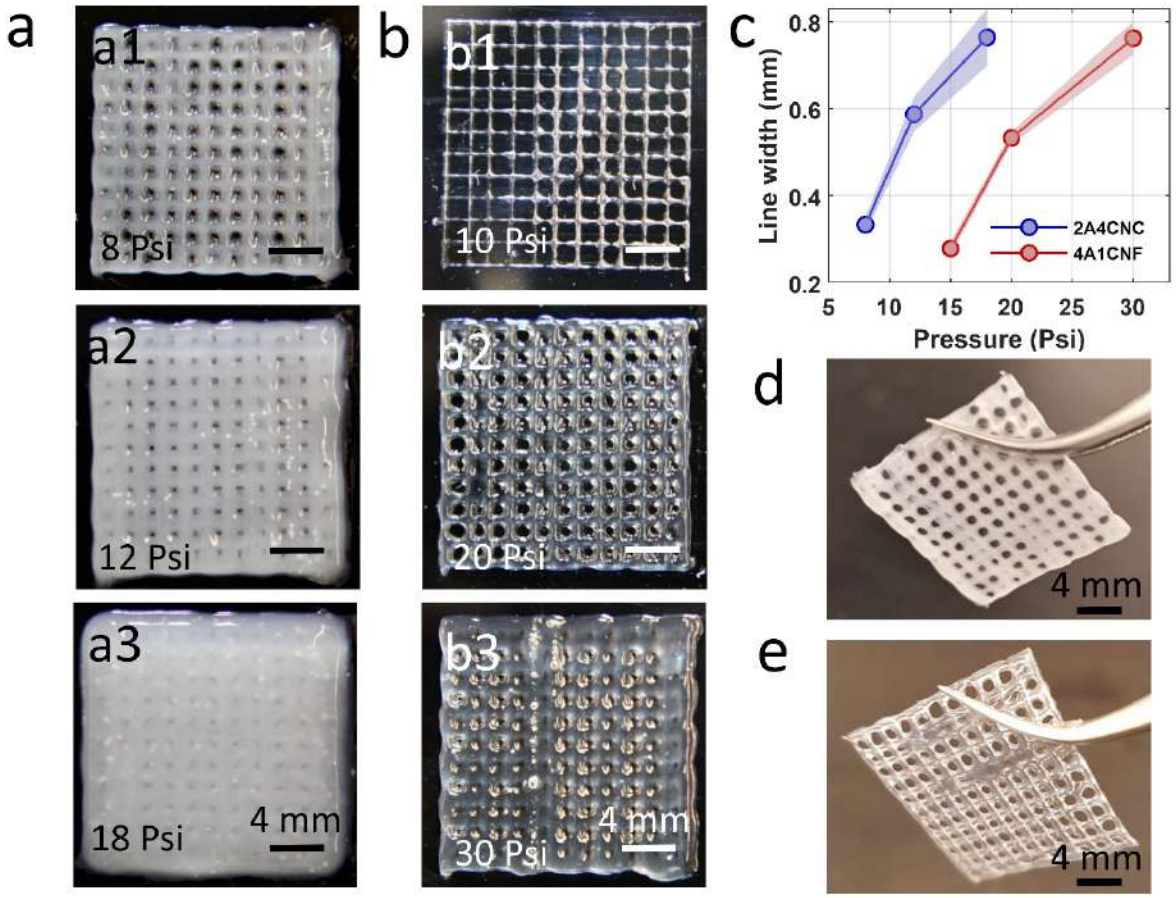

***Figure 3.2. Printability of two hybrid bioink formulations using custom-made bioprinted**. **(a)** Representative images of 3D printed 16-layers and 20 x 20 mm square*

grid pattern for 2A4CNC bioink. Three different air pressures were tested to find optimum pneumatic air pressure. ***(b)*** *Representative images of 3D printed grid pattern with 4A1CNF under three different air pressures.* ***(c)*** *Line thickness that printed by extrusion at various air pressures, showing the effect of air pressure on the filament width.* ***(d)*** *Representative images of 2-layers grid pattern after 2 min cross-linked in calcium with optimum air pressure of 12* psi *for 2A4CNC bioink and* ***(e)*** *optimum air pressure of 20* psi *for 4A1CNF.*

Rheological properties of bioink

Rheological properties of bioinks were characterized to optimize the printability of the proposed bioinks. Fig. 3.3a shows the viscosity measurement results for two hybrid bioinks formulations 4A1CNF, 2A4CNC and their components, 4A, 1CNF, 2A, and 4CNC as a function of shear rate. Both bioinks have higher viscosities than their components, indicating suitability for bioprinting. The curve for pure 2% and 4 % alginate and pure 4% CNC have relatively flat over shear rate, indicating they are not suitable for bioprinting. The measurement of storage modulus, G', and loss modulus, G" of two bioink formulations at frequency sweep of 1 % strain were shown in Fig 3.3b. Storage modulus were higher than loss modulus for both bioink formulations over the angular frequency range of 0-100 rad/s, which indicate that both bioinks are solid-like, and can hold their shape after printing. These results suggest both bioink can have good shape fidelity. 4A1CNF has higher storage modules than 2A4CNC, indicating potential for better shape fidelity. These results are in good agreement with previously reported rheological properties for CNC- and CNF-based bioinks[24,109].

Swelling

Swelling is crucial information for the application of bioink patches because biodegradable patches are usually exposed bodily fluids, such as blood or interstitial fluids during wound healing[110]. The swelling ratios of 3D printed biodegradable patches as a function of time

are shown in Fig. 3.3c. A rapid increase in the swelling was observed after sample immersion, followed by a plateau as maximum water absorbance was reached. After one hour, the swelling percentage of 4A1CNF was found to be 130%, compared with 102% for 2A4CNC. The 4A1CNF sample reached its equilibrium swelling capacity of 158% after 4 hours. No significant increase was observed after 96 hours. 2A4CNC, however, reached maximum swelling percentage of 120% after 8 hours, with no significant change after the full 96 hours. 4A1CNF has higher alginate concentration and larger pore size compared with 2A4CNC's, which could explain the increased water absorbance. It could also be attributed to the larger aspect ratio of nanofiber, compared with that of a nanoparticle[111]. Similar findings reported CNF-alginate hydrogels had higher moisture uptake compared with CNC-alginate hydrogels for both water and PBS[111]. Higher alginate concentrations were also reported to increase swelling percentage[105]. Cellulose nanofibers can be used as an additive material to develop a new patch by customizing its swelling capacity, which may increase the performance of the implantable patch.

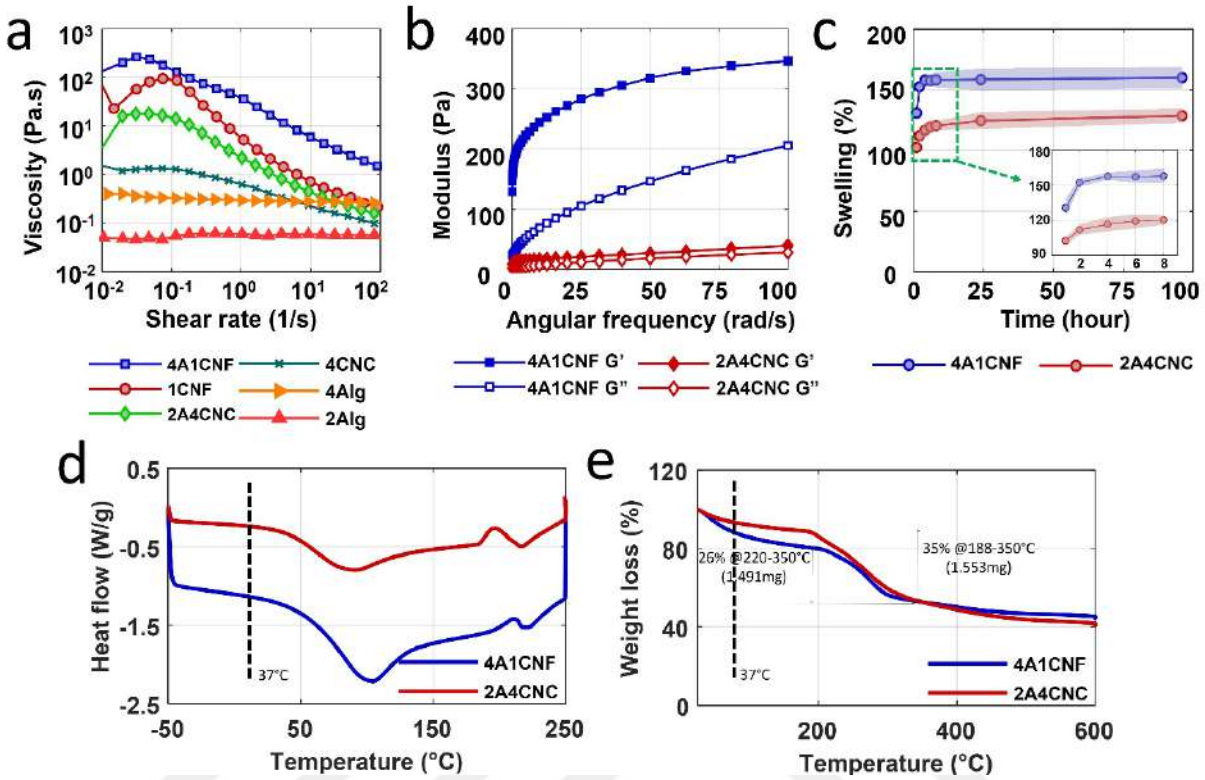

Figure 3.3. Rheological and thermal characterization of bioinks. (a) *Viscosity of two hybrid bioinks formulation 4A1CNF, 2A4CNC and their components, 4A, 1CNF, 2A, and 4CNC as a function of shear rate.* ***(b)*** *Storage modulus (G') and loss modulus (G'') of two bioink formulations 4A1CNF and 2A4CNC.* ***(c)*** *Swelling (water absorbance) of dried patches made with these two bioinks over up to 96 hours. Differential Scanning Calorimetry (DSC) analysis results* ***(d)*** *and Thermogravimetric analysis (TGA) results* ***(e)*** *of freeze-dried 4A1CNF and 2A4CNC samples.*

Thermal analysis

Biodegradable patches are typically prepared at room temperature before being implanted, which would cause a temperature difference. Thermal characterization is helpful to estimate the effect of this change on the patch design. Figure 3.3d shows the results of differential scanning calorimetry (DSC) for both hydrogels. Each hydrogel shows only one endothermic peak (92 °C and 106 °C for 2A4CNC for 4A1CNF, respectively) due to water losses. This endothermic peak is associated with melting temperature. At a body temperature of 37 °C, 4A1CNF has a higher heat flow than 2A4CNC, as seen in Table 3.1, which may be attributed to the higher thermal conductivity

of CNF[106]. Each bioink has one ex-othermic peak (180–210 °C for 2A4CNC, 205–220 °C for 4A1CNF) due to degradation of the bioinks due to water losses.

Thermogravimetric analysis was used to determine thermal stability of CNC and CNF based scaffolds. Fig. 3.3e depicts three major weight losses steps and the thermal degradation. The first step (from 0 °C to 220 °C) is attributed the water evaporation in the hydrogel structure where 2A4CNC had gradual 13% loss of mass until 188°C while there was 20% weight loss toward 220°C in 4A1CNF. The slope of the curve at the body temperature of 37 °C, indicated in Table 3.1, shows 4A1CNF tends towards faster weight loss compared with 2A4CNC. The second step (between 220 and 350 °C) corresponds to the complex degradation and decomposition of glycoside chains in the hydrogels structure. In this step, the weight losses were 35% for 2A4CNC and 26% for 4A1CNF up to 350°C. The last step, both bioinks had constant weight loss from 350 to 600 °C. Two major degradations were occurred at 188 °C and at 350 °C to 2A4CNC and at 220 °C and 350 °C to 4A1CNF due to decomposition of molecular chain in the component of the bioink formulations. The major degradations in 4A1CNF occurred at higher temperatures compared with those of 2A4CNC. This implies that 4A1CNF is more thermally stable than 2A4CNC. This finding agrees with literature, that CNF-alginate hydrogels are more stable than CNC-alginate hydrogels[111]. Additionally, it was also reported that the incorporation of either CNF or CNC in pure alginate was improved the thermal stability of hydrogel when compared the pure alginate[112,105].

Table 3. 1. Thermal characterization results at body temperature of 37 °C.

Samples	Heat flow (W/g) (DSC)	Slope of weight loss (TGA) curve
2A4CNC	-0.3194	-0.176
4A1CNF	-1.2445	-0.277

Mechanical characterization

To help determine how the 3D bioprinted bioinks would perform as flexible and stretchable patches, they were characterized under cycling loading mimicking motion of the skin by uniaxial tensile experiment using DMA. Typical stress-strain curves of both samples are shown in Fig. 3.4c. 4A1CNF has higher tensile strength than 2A4CNC. The tensile strength is 0.26 MPa with a failure strain of 50 % for 4A1CNF, compared with 0.07 MPa and 38 % for 2A4CNC. 4A1CNF is more flexible and more stretchable. Similarly, the average Young's modulus of 4A1CNF (0.45 ± 0.02 MPa) was much higher than 2A4CNC (0.2 ± 0.02 MPa) (Fig. 3.4d). For human skin experiments, failure strain (30-60%)[113] and Young's modulus (0.005-140 MPa) are comparable to the results found for the bioinks[114,115]. Elongation at break is shown in Fig. 3.4e. 4A1CNF is be able to stretche 35% larger than 2A4CNC. As the wrist is one of the most flexed parts of the body with a maximum strain of 22%, these results demonstrates that our proposed custom-made patches are adequate for human body[104].

Both bioinks show relatively linear loading force during the first cycle but nonlinear unloading force over 100 cycles (Fig. 3.4f, g). As restoring strain at zero stress does not return to start after each cycle, proposed patch samples are not 100% elastic, and deform

during loading. The deformation is not large: reaching a maximum deformation of 10% for 2A4CNC after 20 cycles. Maximum deformation for 4A1CNF was 35% lower than 2A4CNC – a mere 6.5%, achieved after 10 cycles. No significant additional deformation was observed afterward after the full 100 cycles for either bioink.

Both bioinks had similar hysteresis during the first cycle, around 5 J. There, however, was some reduction after the first cycle and gradually decreased over 100 cycles (Fig. 3.4h). As the samples did not fully restore to their original length, they did not require as much stretching in subsequent cycles.

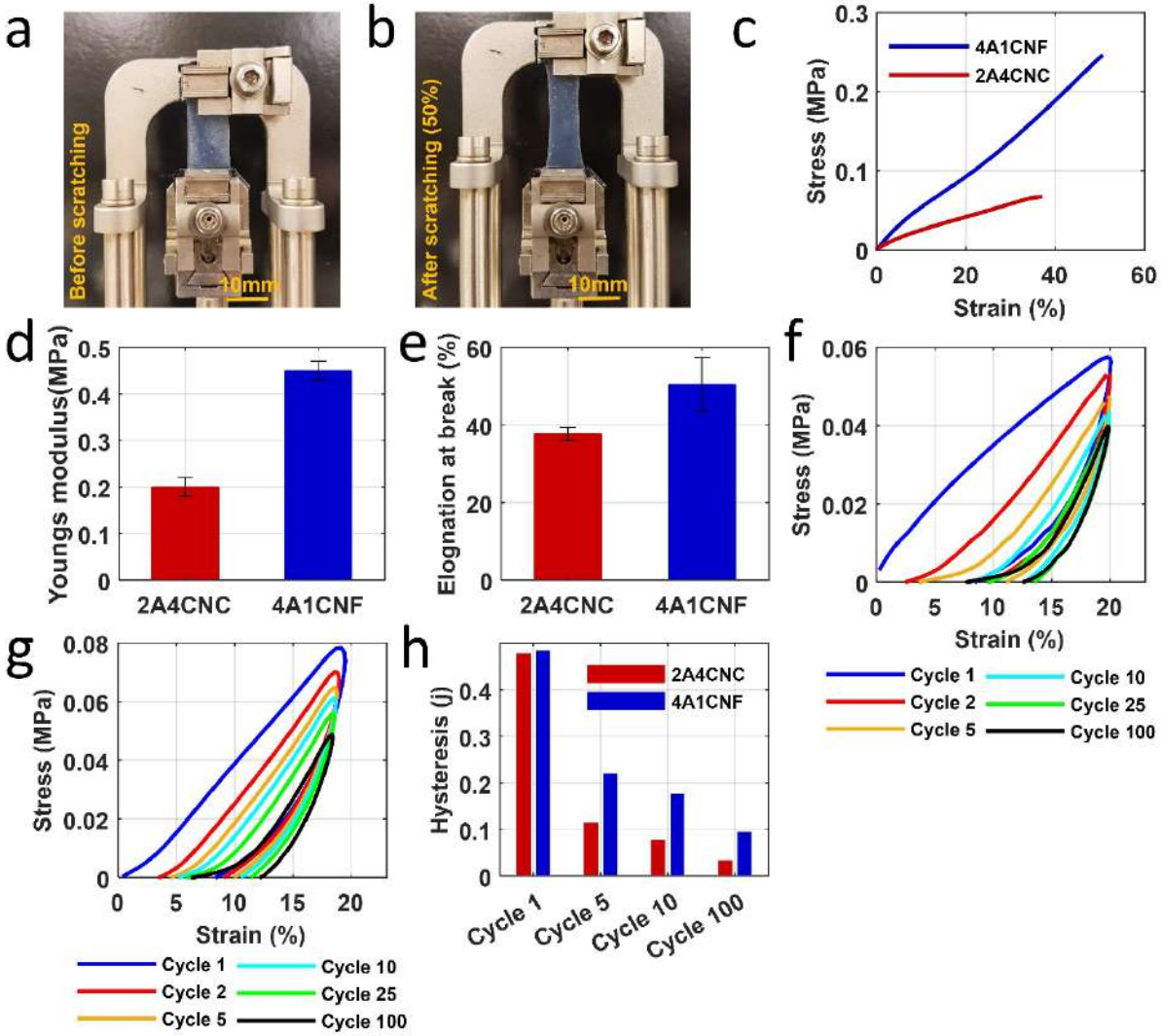

Figure 3.4. Mechanical characterization of 3D printed patches. ***(a, b)*** *Images of 4A1CNF before scratching and 50% elongation under tensile tests.* ***(c)*** *Stress-strain curve of two samples under a ramped fore rate of 0.1 N/min.* ***(d)*** *Young's modulus from the slope in the initial linear region of the stress-strain curve for two samples.* ***(e)*** *Maximum elongation of sample right before the samples fractured. Cycling loading in DI water to assess the hysteresis, deformation over cycling that mimics the movement in the skin for* ***(f)*** *2A4CNC and* ***(g)*** *4A1CNF. The sample was scratched for repeatedly 100 cycles at strain ramp 10%/min to 20% strain.* ***(h)*** *Hysteresis versus number of cycling from the stress-strain curve of inside area of loading and unloading.*

Evaluation of degradation

In vitro degradation properties of 2A4CNC and 4A1CNF are summarized in Fig. 3.5. 4A1CNF showed 30% erosion (weight loss) in cell media within the first two days while 2A4CNC had only 18% degradation over the same time. This is potentially due to that

fiber surface of CNF scaffold, which may be more easily removed compared with 2A4CNC. Following the initial rapid erosion, the weight loss of 4A1CNF slowed and only reached 35% after 20 days. The weight loss of 2A4CNC increased gradually, reaching 45% after 20 days, reaching 90% at the end of 30-day degradation trial, Fig. 3.5a. This high degradation can be attributed to the weak chemical bond with the lower alginate concentration in the hydrogel. The 4A1CNF reached a maximum of 50% after the full 30 days. A similar 50% mass loss over 30 days was reported for the degradation of an alginate-based material[107], with a similar finding reporting that incorporation of CNF in alginate increased resistance against mechanical collapse and degradation. This that CNF-alginate hydrogels have better mechanical stability characteristics compared CNC-alginate hydrogel[111]. Fig. 3.5c shows representative images of washed and freeze-dried samples every 5 days for the duration of the trail. It is worth noting that the 2A4CNC was deformed to degradation, while 4A1CNF maintained most of its shape throughout the degradation.

Mechanical characterization of in vitro degraded samples in the cell culture media was conducted to determine the effect of exposure time on the mechanical properties (Fig. 3.5b). Compressive modulus of the unexposed 2A4CNC and 4A1CNF samples were 0.73 ± 0.08 kPa and 1.2 ± 0.047 kPa, respectively. After degrading for 5 days in media, compressive modulus of the 2A4CNC decreased to 0.066 ± 0.023 kPa while there was no large decrease observed in the compressive modulus of 4A1CNF sample. While the compressive modulus of 4A1CNF decreased sharply to 0.008 ± 0.00 2 kPa over 10 days, it remained 43% higher compared with the compressive modulus of 2A4CNC. Beyond 10 days, there was not any large change in the compressive modulus through the remaining

degradation trail. 4A1CNF had around 120 ± 20% larger compressive modulus than 2A4CNC's through the end of the degradation trials (Fig. 3.5b). The fibrous structure of 4A1CNF may be more resistant to the chemical degradation than crystalline structure of 2A4CNC. Another potential explanation is the higher alginate concentration in 4A1CNF forms stronger chemical bonds, providing improved resistance to heat and chemical degradation compared with lower alginate concentrations, as found in the 2A4CNC sample.

Morphological characterization of 2A4CNC and 4A1CNF samples was conducted, observing detailed pore structures and investigating the effects degradation on the microstructure of samples after 10 days exposure to media. SEM images show changes in the 2A4CNC's crystalline structure and fibrous structure of 4A1CNF with degradation (Fig. 3.5d-f). Samples without degradation showed a porous structures area of 1500 ± 200 μm^2 for 2A4CNC and 5800 ± 1400 μm^2 for 4A1CNF. This result is similar to a previously reported study using alginate-CNC hydrogel, where it was determined that incorporating CNC to pure alginate increased the porosity of hydrogel[103]. A similar finding reported addition of CNF to alginate increased the pore size of hydrogel more than the addition of CNC to alginate[111]. Post degradation, the porous structure area was reduced to 500 ± 350 μm^2 for 2A4CNC and 1200 ± 700 μm^2 for 4A1CNF. After degradation, many pore walls collapsed and pores disappeared. Additionally, the SEM images show that CNC and CNF materials homogenously dispersed in the alginate solution.

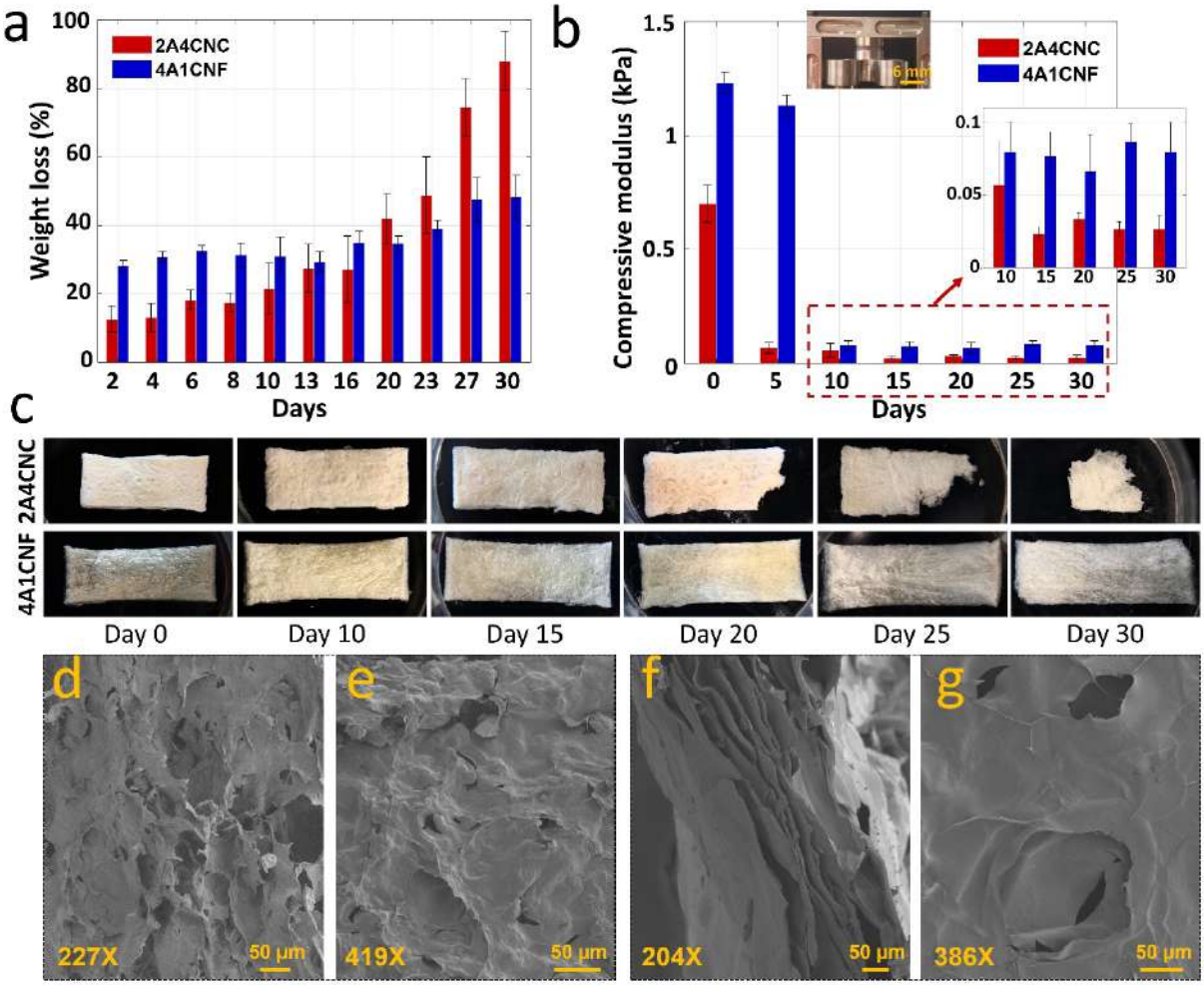

Figure 3.5. In vitro degradation of printed constructs. ***(a)*** *Weight loss (%) of two samples in cell culture media containing Dulbecco's modified Eagle's medium (DMEM) with 10% fatal bovine serum (FBS) over a month.* ***(b)*** *Compressive modulus of samples (10 x 10 mm) was compared with the time of exposure to the cell culture media for 5-day periods up to one month. Inset: a representative image of sample undergoing a compression test by a DMA. Statistical differences calculated by one-way ANAOVA test for multiple comparison ($p<0.0001$).* ***(c)*** *Pictorial representative images of washed and freeze-dried samples after taken from media with 5 days period. Error bars represent the standard deviation of 3 independent measurements. Scanning Electron Microscope (SEM) images of freeze-dried* ***(d)*** *2A4CNC on day 0,* ***(e)*** *2A4CNC after 10-day degradation,* ***(f)*** *4A1CNF on day 0, and* ***(g)*** *4A1CNF after 10-day degradation.*

Cell viability

3T3 mouse embryonic fibroblast cells (National Institutes of Health (NIH)) were combined with the hydrogels and cell viability was observed after ten days using a live/dead assay. Fluorescence images live/dead cell in 2A4CNC hydrogel and 4A1CNF hydrogel are

shown in Fig. 3.6a and b, respectively. Cell viability results from live/dead image analysis for two hydrogels are summarized in Fig. 3.6c. No significant difference was found in cell viability over the first 5 days of the trials for both bioinks, with average viabilities of 83% and 58% for 4A1CNF and 2A4CNC, respectively ($p<0.05$ for both). These results are in agreement with previous studies for alginate-CNC[103], and alginate-CNF[116] bioinks. After 5 days, viability decreased across all samples. This decrease is likely due to competition for oxygen and nutrients. Chemical degradation products entering the cell media could also contribute to this decrease, supported by the sharp decrease in compressive modulus day 5 (Fig. 3.5b). Comparing 4A1CNF to 2A4CNC, the CNF based bioink showed much higher cell viability across all times, with 43% higher viability on day 5 ($p<0.0001$). This could be attributed to the higher alginate concentration in the 4A1CNF bioink which can provide better environment to cell. Another reason might be that, the 4A1CNF hydrogel had a higher swelling ratio, which could increase the nutrients available to the cells. 4A1CNF maintained its dimensional and thermal stability causing high biocompatibility due to the entangled nanofiber network. Consequently, the present cell viability analysis result shows the 4A1CNF hydrogel has a great potential for tissue engineering applications.

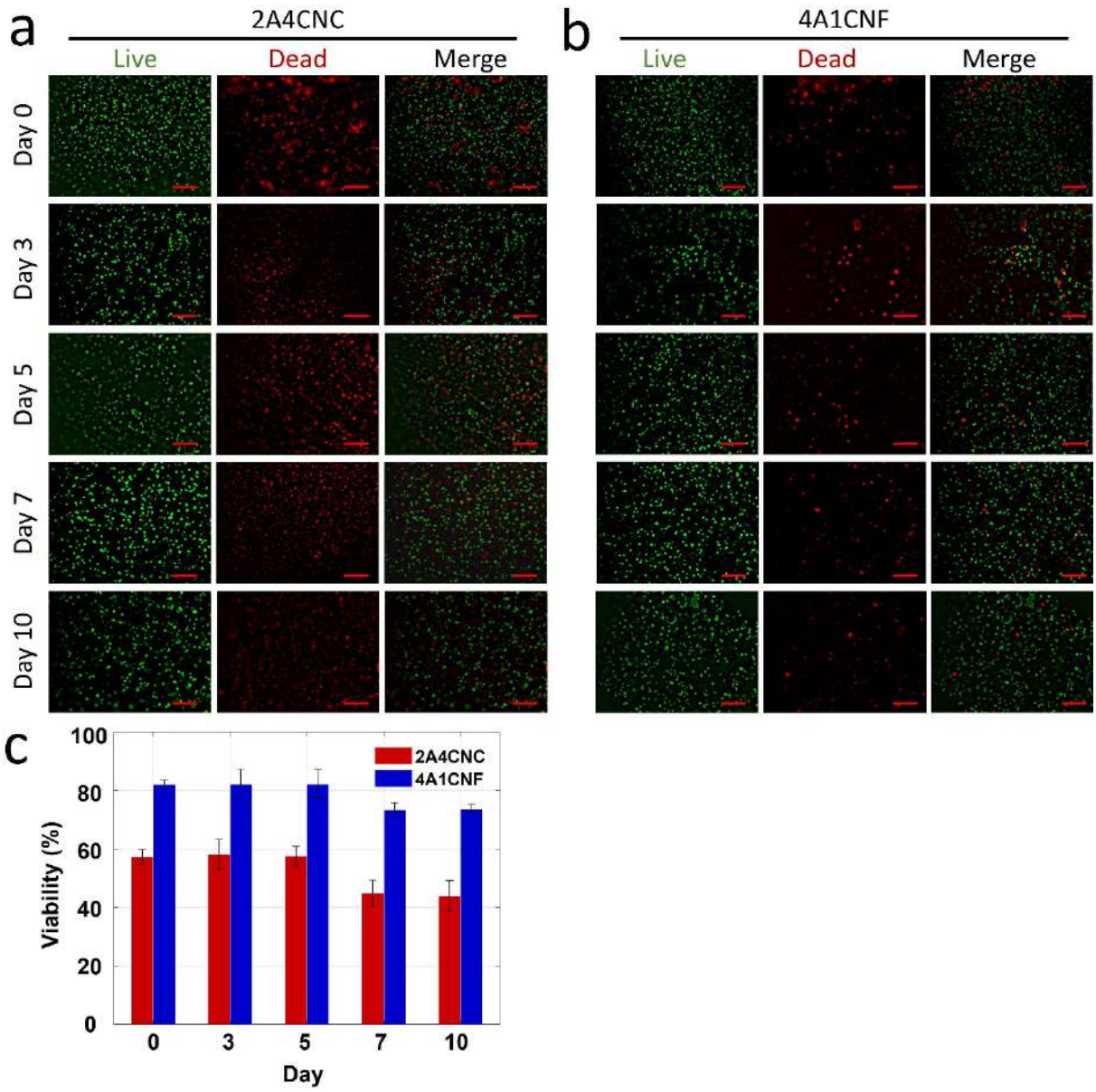

Figure 3.6. Characterization of cell viability. *Fluorescence images of National Institutes of Health (NIH) 3T3 mouse embryonic fibroblast cells in* ***(a)*** *2A4CNC and* ***(b)*** *4A1CNF hydrogels showing the cell viability after day 0, 3, 5, 7, and 10. The green stained (Calcein AM, 0.5μL/mL) cell represents the live cell shown in the first column. Red stained (ethidium homodimer 1, 2μL/mL) cell represents the dead cell shown in the second column. The third column shows the merge of live and dead cells. Scale bar is 500 μm.* ***(c)*** *Quantification of the cell viability from live/dead image analysis. Statistical differences calculated by one-way ANAOVA test and t-test for multiple and two samples comparison ($p<0.0001$). Error bars represents the standard deviation of three independent measurements.*

Conclusion

We developed two hybrid hydrogels by mixing alginate-cellulose nanocrystal and alginate-cellulose nanofibril, and characterized with our custom-made bioprinter. We optimized parameters for each of the hydrogels for 3D printing, including material concentration, print speed, and nozzle pressure to achieve best shape fidelity. CNC has been previously demonstrated for reinforcing alginate-based hydrogels. We demonstrate that CNF as an additive increases the tolerance of the bioink to physical deformation compared with CNC. 4A1CNF had a 10% further elongation before breaking and increased the Youngs Modulus to 0.45 MPa compared with 2A4CNC's 0.2 MPa. Further, the CNF bioink has nearly double the compressive modulus at 1.25 kPa compared with the CNC bioink's of 0.7 kPa. 2A1CNF is also much more stable under biodegradation conditions, maintaining a weight loss between 30 and 50%, compared with 2A4CNC varying from 14% to 87% over the course of the 30-day experiment. Finally, to validate our proposed materials for the tissue engineering, we characterized cell viability of NIH 3T3 mouse fibroblast cell over time. 4A1CNF demonstrated more than 20% higher cell viability across all times, compared with 2A4CNC. Overall, we demonstrate CNF as a promising additive material for bioink patches because of its better printability, higher mechanical and rheological properties including, viscosity, Young's and comprehensive modulus. The morphological structure of 4A1CNF has larger porosity that provides is high liquid absorbency and chemical durability against cell media. Also, it shows excellent chemical and shape fidelity preserving its shape over the 30-day degradation. Additionally, 4A1CNC exhibits better biocompatibility.

CONCLUSION

This thesis introduced fidelity analysis of biodegradable patch made with a low-cost and high-throughput custom-made bioprinting. At the first step, a low-cost hybrid droplet-and-extrusion-based bioprinter was developed to address the increasing demand for readily available biomimetic tissues and organs. This bioprinter is capable of direct-write bioprinting of hydrogel material in multiple layers balancing both high-resolution (using the inkjet head and photo-crosslinking) and high-throughput (using the extrusion head and chemical-crosslinking). The effectiveness of both modes of printing in various 2D and 3D custom designs and structures were characterized using commercially available and widely used two hydrogels, GelMA and alginate for the inkjet and extrusion printing, respectively. To validate this approach for tissue engineering, we characterized the cell viability of mouse fibroblast cells over time. Furthermore, our platform can be benchmarked for other hydrogels and polymers, in addition to the GelMA and alginate reported, by adjusting the printer settings and parameters, such as the rate of extrusion and the droplet dispensing timing and pressure.

Then, two shape fidelity experimental analysis techniques were proposed and a mathematical model supportive of one of these was developed. The developed bioprinter and commercially available bioink materials of alginate and gelatin were used to run these techniques. These methods are readily accessible and replicable techniques to easily test a new bioink formulation. It can help to accelerate the development process of a new bioink by evaluating its performance for shape fidelity. By considering the accessibility and repeatability, these methods highly suitable for testing the new bioink materials.

At the next step, 3D bioprinted biodegradable patches to be implanted on real human tissue were analyzed for shape, mechanical and chemical fidelity to improve their functionality. Two hybrid hydrogels were developed to bioprint these patches by mixing alginate-CNC and alginate-CNF and characterized with the developed custom-made bioprinter. The printing parameters were optimized for each of the hydrogels for 3D printing, including material concentration, print speed, and nozzle pressure to achieve best shape fidelity. Rheological and mechanical characterization were conducted to determine mechanical fidelity, by performing mechanic analysis and cyclic loading. Chemical fidelity analysis was performed via cell culture media exposure to observe biodegradability of bioink patches with time. Finally, biocompatibility of the hydrogels was tested by cell viability analysis. It was found that CNF is promising additive material for bioink patches because of its better printability, biocompatibility, and higher mechanical and rheological properties including, viscosity, and Young's modulus.

Overall, a low-cost, high-throughput custom-made bioprinter was developed to 3D bioprint a biodegradable patch. Fidelity analysis of a patch including shape, mechanical and chemical fidelity were performed as well as the biocompatibility of hydrogel.

REFERENCES

1. Collection AS. Tissue engineering. *J Cell Biochem*. 2005;44(S14E):227-256. doi:10.1002/jcb.240440806

2. Torikai K, Ichikawa H, Hirakawa K, et al. A self-renewing, tissue-engineered vascular graft for arterial reconstruction. *J Thorac Cardiovasc Surg*. 2008;136(1):7-11. doi:10.1016/j.jtcvs.2007.06.039

3. Hutmacher DW. Scaffolds in tissue engineering bone and cartilage. *Biomater Silver Jubil Compend*. 2006;21:175-189. doi:10.1016/B978-008045154-1.50021-6

4. Zhao X, Sun X, Yildirimer L, et al. HHS Public Access. Published online 2018:66-77. doi:10.1016/j.actbio.2016.11.017.Cell

5. Fujimoto KL, Guan J, Oshima H, Sakai T, Wagner WR. In Vivo Evaluation of a Porous, Elastic, Biodegradable Patch for Reconstructive Cardiac Procedures. *Ann Thorac Surg*. 2007;83(2):648-654. doi:10.1016/j.athoracsur.2006.06.085

6. Boutry CM, Beker L, Kaizawa Y, et al. Biodegradable and flexible arterial-pulse sensor for the wireless monitoring of blood flow. *Nat Biomed Eng*. 2019;3(1):47-57. doi:10.1038/s41551-018-0336-5

7. Tamayol A, Hassani Najafabadi A, Mostafalu P, et al. Biodegradable elastic nanofibrous platforms with integrated flexible heaters for on-demand drug delivery. *Sci Rep*. 2017;7(1):1-10. doi:10.1038/s41598-017-04749-8

8. Sousa MP, Neto AI, Correia TR, et al. Bioinspired multilayer membranes as potential adhesive patches for skin wound healing. *Biomater Sci*. 2018;6(7):1962-1975. doi:10.1039/c8bm00319j

9. Herndon DN. *Total Burn Care*.; 2007. doi:10.1016/B978-1-4160-3274-8.X5001-6

10. Shinoka T, Shum-Tim D, Ma PX, et al. Creation of viable pulmonary artery autografts through tissue engineering. *J Thorac Cardiovasc Surg*. 1998;115(3):536-546. doi:10.1016/S0022-5223(98)70315-0

11. D'Amore A, Yoshizumi T, Luketich SK, et al. Bi-layered polyurethane – Extracellular

matrix cardiac patch improves ischemic ventricular wall remodeling in a rat model. *Biomaterials*. 2016;107:1-14. doi:10.1016/j.biomaterials.2016.07.039

12. Zhang X, Zhang Y. Tissue Engineering Applications of Three-Dimensional Bioprinting. *Cell Biochem Biophys*. 2015;72(3):777-782. doi:10.1007/s12013-015-0531-x

13. Axpe E, Oyen ML. Applications of Alginate-Based Bioinks in 3D Bioprinting. *Int J Mol Sci*. 2016;17(12). doi:10.3390/ijms17121976

14. Li L, Qin S, Peng J, et al. Engineering gelatin-based alginate/carbon nanotubes blend bioink for direct 3D printing of vessel constructs. *Int J Biol Macromol*. 2020;145:262-271. doi:10.1016/j.ijbiomac.2019.12.174

15. Yue K, Trujillo-de Santiago G, Alvarez MM, Tamayol A, Annabi N, Khademhosseini A. Synthesis, properties, and biomedical applications of gelatin methacryloyl (GelMA) hydrogels. *Biomaterials*. 2015;73:254-271. doi:10.1016/j.biomaterials.2015.08.045

16. Liu T, Weng W, Zhang Y, Sun X, Yang H. Applications of Gelatin Methacryloyl (GelMA) Hydrogels in Microfluidic Technique-Assisted Tissue Engineering. *Molecules*. 2020;25(22). doi:10.3390/molecules25225305

17. Rastogi P, Kandasubramanian B. Review of alginate-based hydrogel bioprinting for application in tissue engineering. *Biofabrication*. 2019;11(4). doi:10.1088/1758-5090/ab331e

18. Athukoralalage SS, Balu R, Dutta NK, Roy Choudhury N. 3D Bioprinted

Nanocellulose-Based Hydrogels for Tissue Engineering Applications: A Brief Review. *Polymers (Basel)*. 2019;11(5):898. doi:10.3390/polym11050898

19. Leppiniemi J, Lahtinen P, Paajanen A, et al. 3D-Printable Bioactivated Nanocellulose-Alginate Hydrogels. *ACS Appl Mater Interfaces*. 2017;9(26):21959-21970. doi:10.1021/acsami.7b02756

20. Habibi Y, Lucia LA, Rojas OJ. Cellulose nanocrystals: Chemistry, self-assembly, and applications. *Chem Rev*. 2010;110(6):3479-3500. doi:10.1021/cr900339w

21. Klemm D, Kramer F, Moritz S, et al. Nanocelluloses: A new family of nature-based materials. *Angew Chemie - Int Ed*. 2011;50(24):5438-5466. doi:10.1002/anie.201001273

22. Luo H, Cha R, Li J, Hao W, Zhang Y, Zhou F. Advances in tissue engineering of nanocellulose-based scaffolds: A review. *Carbohydr Polym*. 2019;224(July):115144. doi:10.1016/j.carbpol.2019.115144

23. Ma X, Li R, Zhao X, et al. Biopolymer composite fibres composed of calcium alginate reinforced with nanocrystalline cellulose. *Compos Part A Appl Sci Manuf*. 2017;96:155-163. doi:10.1016/j.compositesa.2017.02.021

24. Markstedt K, Mantas A, Tournier I, Martínez Ávila H, Hägg D, Gatenholm P. 3D bioprinting human chondrocytes with nanocellulose-alginate bioink for cartilage tissue engineering applications. *Biomacromolecules*. 2015;16(5):1489-1496. doi:10.1021/acs.biomac.5b00188

25. Ajdary R, Huan S, Zanjanizadeh Ezazi N, et al. Acetylated Nanocellulose for Single-

Component Bioinks and Cell Proliferation on 3D-Printed Scaffolds. *Biomacromolecules*. 2019;20(7):2770-2778. doi:10.1021/acs.biomac.9b00527

26. Knowlton S, Tasoglu S. A Bioprinted Liver-on-a-Chip for Drug Screening Applications. *Trends Biotechnol*. 2016;34(9):681-682. doi:10.1016/j.tibtech.2016.05.014

27. Knowlton S, Yenilmez B, Tasoglu S. Towards Single-Step Biofabrication of Organs on a Chip via 3D Printing. *Trends Biotechnol*. 2016;34(9):685-688. doi:10.1016/j.tibtech.2016.06.005

28. Knowlton S, Onal S, Yu CH, Zhao JJ, Tasoglu S. Bioprinting for cancer research. *Trends Biotechnol*. 2015;33(9):504-513. doi:10.1016/j.tibtech.2015.06.007

29. Memic A, Navaei A, Mirani B, et al. Bioprinting technologies for disease modeling. *Biotechnol Lett*. 2017;39(9):1279-1290. doi:10.1007/s10529-017-2360-z

30. Kang HW, Lee SJ, Ko IK, Kengla C, Yoo JJ, Atala A. A 3D bioprinting system to produce human-scale tissue constructs with structural integrity. *Nat Biotechnol*. 2016;34(3):312-319. doi:10.1038/nbt.3413

31. Liaw CY, Ji S, Guvendiren M. Engineering 3D Hydrogels for Personalized In Vitro Human Tissue Models. *Adv Healthc Mater*. 2018;7(4):1-16. doi:10.1002/adhm.201701165

32. 3D Bioprinting in Regenerative Engineering: Principles and Application. Accessed December 14, 2020. https://www.routledge.com/3D-Bioprinting-in-Regenerative-Engineering-Principles-and-Applications/Khademhosseini-Camci-

Unal/p/book/9781138197176

33. Tasoglu S, Demirci U. Bioprinting for stem cell research. *Trends Biotechnol*. 2013;31(1):10-19. doi:10.1016/j.tibtech.2012.10.005

34. Knowlton S, Yu CH, Ersoy F, Emadi S, Khademhosseini A, Tasoglu S. 3D-printed microfluidic chips with patterned, cell-laden hydrogel constructs. *Biofabrication*. 2016;8(2):025019. doi:10.1088/1758-5090/8/2/025019

35. Knowlton S, Li D, Ersoy F, Cho YK, Tasoglu S. Building blocks for bottom-up neural tissue engineering: Tools for in vitro assembly and interrogation of neural circuits. In: *Neural Engineering: From Advanced Biomaterials to 3D Fabrication Techniques*. Springer International Publishing; 2016:123-144. doi:10.1007/978-3-319-31433-4_4

36. Zhou M, Hoon Lee B, Poh Tan L. A dual crosslinking strategy to tailor rheological properties of gelatin methacryloyl. *Int J Bioprinting*. 2017;3(2). doi:10.18063/IJB.2017.02.003

37. Jia W, Gungor-Ozkerim PS, Zhang YS, et al. Direct 3D bioprinting of perfusable vascular constructs using a blend bioink. *Biomaterials*. 2016;106. doi:10.1016/j.biomaterials.2016.07.038

38. Knowlton S, Yenilmez B, Anand S, Tasoglu S. Photocrosslinking-based bioprinting: Examining crosslinking schemes. *Bioprinting*. 2017;5(February 2019):10-18. doi:10.1016/j.bprint.2017.03.001

39. Lepowsky E, Muradoglu M, Tasoglu S. Towards preserving post-printing cell

viability and improving the resolution: Past, present, and future of 3D bioprinting theory. *Bioprinting*. 2018;11(July):1-17. doi:10.1016/j.bprint.2018.e00034

40. Murphy S V., Atala A. 3D bioprinting of tissues and organs. *Nat Biotechnol*. 2014;32(8):773-785. doi:10.1038/nbt.2958

41. Peppas NA, Hilt JZ, Khademhosseini A, Langer R. Hydrogels in biology and medicine: From molecular principles to bionanotechnology. *Adv Mater*. 2006;18(11):1345-1360. doi:10.1002/adma.200501612

42. Slaughter B V., Khurshid SS, Fisher OZ, Khademhosseini A, Peppas NA. Hydrogels in regenerative medicine. *Adv Mater*. 2009;21(32-33):3307-3329. doi:10.1002/adma.200802106

43. Nichol JW, Koshy ST, Bae H, Hwang CM, Yamanlar S, Khademhosseini A. Cell-laden microengineered gelatin methacrylate hydrogels. *Biomaterials*. 2010;31(21):5536-5544. doi:10.1016/j.biomaterials.2010.03.064

44. Bertassoni LE, Cardoso JC, Manoharan V, et al. Direct-write bioprinting of cell-laden methacrylated gelatin hydrogels. *Biofabrication*. 2014;6(2). doi:10.1088/1758-5082/6/2/024105

45. Kolesky DB, Truby RL, Gladman AS, Busbee TA, Homan KA, Lewis JA. 3D bioprinting of vascularized, heterogeneous cell-laden tissue constructs. *Adv Mater*. 2014;26(19):3124-3130. doi:10.1002/adma.201305506

46. Zhu W, Harris BT, Zhang LG. Gelatin methacrylamide hydrogel with graphene nanoplatelets for neural cell-laden 3D bioprinting. *Proc Annu Int Conf IEEE Eng*

Med Biol Soc EMBS. 2016;2016-Octob:4185-4188. doi:10.1109/EMBC.2016.7591649

47. Augst AD, Kong HJ, Mooney DJ. Alginate hydrogels as biomaterials. *Macromol Biosci*. 2006;6(8):623-633. doi:10.1002/mabi.200600069

48. Bendtsen ST, Quinnell SP, Wei M. Development of a novel alginate-polyvinyl alcohol-hydroxyapatite hydrogel for 3D bioprinting bone tissue engineered scaffolds. *J Biomed Mater Res - Part A*. 2017;105(5):1457-1468. doi:10.1002/jbm.a.36036

49. Park J, Lee SJ, Chung S, et al. Cell-laden 3D bioprinting hydrogel matrix depending on different compositions for soft tissue engineering: Characterization and evaluation. *Mater Sci Eng C*. 2017;71:678-684. doi:10.1016/j.msec.2016.10.069

50. Schütz K, Placht AM, Paul B, Brüggemeier S, Gelinsky M, Lode A. Three-dimensional plotting of a cell-laden alginate/methylcellulose blend: towards biofabrication of tissue engineering constructs with clinically relevant dimensions. *J Tissue Eng Regen Med*. 2017;11(5):1574-1587. doi:10.1002/term.2058

51. Fairbanks BD, Schwartz MP, Bowman CN, Anseth KS. Photoinitiated polymerization of PEG-diacrylate with lithium phenyl-2,4,6-trimethylbenzoylphosphinate: polymerization rate and cytocompatibility. *Biomaterials*. 2009;30(35):6702-6707. doi:10.1016/j.biomaterials.2009.08.055

52. Gao Q, He Y, Fu J zhong, Liu A, Ma L. Coaxial nozzle-assisted 3D bioprinting with built-in microchannels for nutrients delivery. *Biomaterials*. 2015;61:203-215. doi:10.1016/j.biomaterials.2015.05.031

53. Colosi C, Costantini M, Barbetta A, Dentini M. Microfluidic bioprinting of heterogeneous 3d tissue constructs. *Methods Mol Biol*. 2017;1612:369-380. doi:10.1007/978-1-4939-7021-6_26

54. Dai X, Liu L, Ouyang J, et al. Coaxial 3D bioprinting of self-assembled multicellular heterogeneous tumor fibers. *Sci Rep*. 2017;7(1):1-12. doi:10.1038/s41598-017-01581-y

55. Liu W, Zhong Z, Hu N, et al. Coaxial extrusion bioprinting of 3D microfibrous constructs with cell-favorable gelatin methacryloyl microenvironments. *Biofabrication*. 2018;10(2). doi:10.1088/1758-5090/aa9d44

56. Schneider CA, Rasband WS, Eliceiri KW. NIH Image to ImageJ: 25 years of image analysis. *Nat Methods*. 2012;9(7):671-675. doi:10.1038/nmeth.2089

57. Guillotin B, Souquet A, Catros S, et al. Laser assisted bioprinting of engineered tissue with high cell density and microscale organization. *Biomaterials*. 2010;31(28):7250-7256. doi:10.1016/j.biomaterials.2010.05.055

58. Nakamura M, Kobayashi A, Takagi F, et al. Biocompatible Inkjet Printing Technique for Designed Seeding of Individual Living Cells. *Tissue Eng*. 2005;11(11-12):1658-1666. doi:10.1089/ten.2005.11.1658

59. Wang Z, Abdulla R, Parker B, Samanipour R, Ghosh S, Kim K. A simple and high-resolution stereolithography-based 3D bioprinting system using visible light crosslinkable bioinks. *Biofabrication*. 2015;7(4). doi:10.1088/1758-5090/7/4/045009

60. Demirci U, Montesano G. Single cell epitaxy by acoustic picolitre droplets. *Lab Chip*. 2007;7(9):1139-1145. doi:10.1039/b704965j

61. Droplets CH, Moon S, Ph D, Hasan SK, Song YS, Ph D. Layer by Layer Three-Dimensional Tissue. 2010;16(1).

62. Ozbolat IT, Hospodiuk M. Current advances and future perspectives in extrusion-based bioprinting. *Biomaterials*. 2016;76:321-343. doi:10.1016/j.biomaterials.2015.10.076

63. Liu W, Zhang YS, Heinrich MA, et al. Rapid Continuous Multimaterial Extrusion Bioprinting. *Adv Mater*. 2017;29(3):1-8. doi:10.1002/adma.201604630

64. Yan Y, Wang X, Pan Y, et al. Fabrication of viable tissue-engineered constructs with 3D cell-assembly technique. *Biomaterials*. 2005;26(29):5864-5871. doi:10.1016/j.biomaterials.2005.02.027

65. Miller JS, Stevens KR, Yang MT, et al. Rapid casting of patterned vascular networks for perfusable engineered three-dimensional tissues. *Nat Mater*. 2012;11(9):768-774. doi:10.1038/nmat3357

66. Hong S, Song SJ, Lee JY, et al. Cellular behavior in micropatterned hydrogels by bioprinting system depended on the cell types and cellular interaction. *J Biosci Bioeng*. 2013;116(2):224-230. doi:10.1016/j.jbiosc.2013.02.011

67. Serex L, Bertsch A, Renaud P. Microfluidics: A new layer of control for extrusion-based 3D printing. *Micromachines*. 2018;9(2). doi:10.3390/mi9020086

68. Derakhshanfar S, Mbeleck R, Xu K, Zhang X, Zhong W, Xing M. 3D bioprinting for

biomedical devices and tissue engineering: A review of recent trends and advances. *Bioact Mater*. 2018;3(2):144-156. doi:10.1016/j.bioactmat.2017.11.008

69. Gillispie G, Prim P, Copus J, et al. Assessment methodologies for extrusion-based bioink printability. *Biofabrication*. 2020;12(2):1-28. doi:10.1088/1758-5090/ab6f0d

70. Ribeiro A, Blokzijl MM, Levato R, et al. Assessing bioink shape fidelity to aid material development in 3D bioprinting. *Biofabrication*. 2017;10(1):014102. doi:10.1088/1758-5090/aa90e2

71. Ozbolat IT, Hospodiuk M. Current advances and future perspectives in extrusion-based bioprinting. *Biomaterials*. 2016;76:321-343. doi:10.1016/j.biomaterials.2015.10.076

72. Schwab A, Levato R, D'Este M, Piluso S, Eglin D, Malda J. Printability and Shape Fidelity of Bioinks in 3D Bioprinting. *Chem Rev*. 2020;120(19):11028-11055. doi:10.1021/acs.chemrev.0c00084

73. He Y, Yang F, Zhao H, Gao Q, Xia B, Fu J. Research on the printability of hydrogels in 3D bioprinting. *Sci Rep*. 2016;6(1):29977. doi:10.1038/srep29977

74. Mouser VHM, Levato R, Mensinga A, Dhert WJA, Gawlitta D, Malda J. Bio-ink development for three-dimensional bioprinting of hetero-cellular cartilage constructs. *Connect Tissue Res*. 2020;61(2):137-151. doi:10.1080/03008207.2018.1553960

75. Ouyang L, Yao R, Zhao Y, Sun W. Effect of bioink properties on printability and cell viability for 3D bioplotting of embryonic stem cells. *Biofabrication*. 2016;8(3).

doi:10.1088/1758-5090/8/3/035020

76. Petta D, Grijpma DW, Alini M, Eglin D, D'Este M. Three-Dimensional Printing of a Tyramine Hyaluronan Derivative with Double Gelation Mechanism for Independent Tuning of Shear Thinning and Postprinting Curing. *ACS Biomater Sci Eng*. 2018;4(8):3088-3098. doi:10.1021/acsbiomaterials.8b00416

77. Paxton N, Smolan W, Böck T, Melchels F, Groll J, Jungst T. Proposal to assess printability of bioinks for extrusion-based bioprinting and evaluation of rheological properties governing bioprintability. *Biofabrication*. 2017;9(4). doi:10.1088/1758-5090/aa8dd8

78. Peak CW, Stein J, Gold KA, Gaharwar AK. Nanoengineered Colloidal Inks for 3D Bioprinting. *Langmuir*. 2018;34(3):917-925. doi:10.1021/acs.langmuir.7b02540

79. Sarker M, Chen XB. Modeling the Flow Behavior and Flow Rate of Medium Viscosity Alginate for Scaffold Fabrication With a Three-Dimensional Bioplotter. *J Manuf Sci Eng Trans ASME*. 2017;139(8):1-14. doi:10.1115/1.4036226

80. Jungst T, Smolan W, Schacht K, Scheibel T, Groll J. Strategies and Molecular Design Criteria for 3D Printable Hydrogels. *Chem Rev*. 2016;116(3):1496-1539. doi:10.1021/acs.chemrev.5b00303

81. Zhao Y, Li Y, Mao S. Effect of bioink properties on printability and cell viability for 3D bioplotting of embryonic stem cells The influence of printing parameters on cell survival rate and printability in microextrusion-based 3D cell printing technology. *Biofabrication*. 2016;8(035020). http://iopscience.iop.org/1758-5090/8/3/035020

82. Duan B, Hockaday LA, Kang KH, Butcher JT. 3D Bioprinting of heterogeneous aortic valve conduits with alginate/gelatin hydrogels. *J Biomed Mater Res - Part A*. 2013;101 A(5):1255-1264. doi:10.1002/jbm.a.34420

83. Yao R, Zhang R, Luan J, Lin F. Alginate and alginate/gelatin microspheres for human adipose-derived stem cell encapsulation and differentiation. *Biofabrication*. 2012;4(2). doi:10.1088/1758-5082/4/2/025007

84. Rhee S, Puetzer JL, Mason BN, Reinhart-King CA, Bonassar LJ. 3D Bioprinting of Spatially Heterogeneous Collagen Constructs for Cartilage Tissue Engineering. *ACS Biomater Sci Eng*. 2016;2(10):1800-1805. doi:10.1021/acsbiomaterials.6b00288

85. Sahranavard M, Zamanian A, Ghorbani F, Shahrezaee MH. A critical review on three dimensional-printed chitosan hydrogels for development of tissue engineering. *Bioprinting*. 2020;17(September 2019):e00063. doi:10.1016/j.bprint.2019.e00063

86. Van Den Bulcke AI, Bogdanov B, De Rooze N, Schacht EH, Cornelissen M, Berghmans H. Structural and rheological properties of methacrylamide modified gelatin hydrogels. *Biomacromolecules*. 2000;1(1):31-38. doi:10.1021/bm990017d

87. Yenilmez B, Temirel M, Knowlton S, Lepowsky E, Tasoglu S. Development and characterization of a low-cost 3D bioprinter. *Bioprinting*. 2019;13. doi:10.1016/j.bprint.2019.e00044

88. Therriault D, White SR, Lewis JA. Rheological behavior of fugitive organic inks for direct-write assembly. *Appl Rheol*. 2007;17(1):1-8. doi:10.1515/arh-2007-0001

89. Smandri A, Nordin A, Hwei NM, Chin KY, Abd Aziz I, Fauzi MB. Natural 3D-printed bioinks for skin regeneration and wound healing: A systematic review. *Polymers (Basel)*. 2020;12(8). doi:10.3390/polym12081782

90. Albanna M, Binder KW, Murphy S V., et al. In Situ Bioprinting of Autologous Skin Cells Accelerates Wound Healing of Extensive Excisional Full-Thickness Wounds. *Sci Rep*. 2019;9(1):1-15. doi:10.1038/s41598-018-38366-w

91. Liu J, Chi J, Wang K, Liu X, Liu J, Gu F. Full-thickness wound healing using 3D bioprinted gelatin-alginate scaffolds in mice: A histopathological study. *Int J Clin Exp Pathol*. 2016;9(11):11197-11205.

92. Xu W, Molino BZ, Cheng F, et al. On Low-Concentration Inks Formulated by Nanocellulose Assisted with Gelatin Methacrylate (GelMA) for 3D Printing toward Wound Healing Application. *ACS Appl Mater Interfaces*. 2019;11(9):8838-8848. doi:10.1021/acsami.8b21268

93. Nocera AD, Comín R, Salvatierra NA, Cid MP. Development of 3D printed fibrillar collagen scaffold for tissue engineering. *Biomed Microdevices*. 2018;20(2):1-13. doi:10.1007/s10544-018-0270-z

94. Karavasili C, Tsongas K, Andreadis II, et al. Physico-mechanical and finite element analysis evaluation of 3D printable alginate-methylcellulose inks for wound healing applications. *Carbohydr Polym*. 2020;247(June):116666. doi:10.1016/j.carbpol.2020.116666

95. Kim BS, Kwon YW, Kong JS, et al. 3D cell printing of in vitro stabilized skin model and in vivo pre-vascularized skin patch using tissue-specific extracellular matrix

bioink: A step towards advanced skin tissue engineering. *Biomaterials*. 2018;168:38-53. doi:10.1016/j.biomaterials.2018.03.040

96. Chen CS, Zeng F, Xiao X, et al. Three-Dimensionally Printed Silk-Sericin-Based Hydrogel Scaffold: A Promising Visualized Dressing Material for Real-Time Monitoring of Wounds. *ACS Appl Mater Interfaces*. 2018;10(40):33879-33890. doi:10.1021/acsami.8b10072

97. Xiong S, Zhang X, Lu P, et al. A Gelatin-sulfonated Silk Composite Scaffold based on 3D Printing Technology Enhances Skin Regeneration by Stimulating Epidermal Growth and Dermal Neovascularization. *Sci Rep*. 2017;7(1):1-12. doi:10.1038/s41598-017-04149-y

98. Wang X, Wang Q, Xu C. Nanocellulose-based inks for 3d bioprinting: Key aspects in research development and challenging perspectives in applications—a mini review. *Bioengineering*. 2020;7(2). doi:10.3390/bioengineering7020040

99. Mancha Sánchez E, Gómez-Blanco JC, López Nieto E, et al. Hydrogels for Bioprinting: A Systematic Review of Hydrogels Synthesis, Bioprinting Parameters, and Bioprinted Structures Behavior. *Front Bioeng Biotechnol*. 2020;8(August). doi:10.3389/fbioe.2020.00776

100. Zainal SH, Mohd NH, Suhaili N, Anuar FH, Lazim AM, Othaman R. Preparation of cellulose-based hydrogel: a review. *J Mater Res Technol*. 2021;10:935-952. doi:10.1016/j.jmrt.2020.12.012

101. Unagolla JM, Jayasuriya AC. Hydrogel-based 3D bioprinting: A comprehensive review on cell-laden hydrogels, bioink formulations, and future perspectives. *Appl*

Mater Today. 2020;18:100479. doi:10.1016/j.apmt.2019.100479

102. Heid S, Boccaccini AR. Advancing bioinks for 3D bioprinting using reactive fillers: A review. *Acta Biomater*. 2020;113:1-22. doi:10.1016/j.actbio.2020.06.040

103. Wu Y, Lin ZY (William), Wenger AC, Tam KC, Tang X (Shirley). 3D bioprinting of liver-mimetic construct with alginate/cellulose nanocrystal hybrid bioink. *Bioprinting*. 2018;9(December 2017):1-6. doi:10.1016/j.bprint.2017.12.001

104. Lu N, Lu C, Yang S, Rogers J. Highly sensitive skin-mountable strain gauges based entirely on elastomers. *Adv Funct Mater*. 2012;22(19):4044-4050. doi:10.1002/adfm.201200498

105. Huq T, Salmieri S, Khan A, et al. Nanocrystalline cellulose (NCC) reinforced alginate based biodegradable nanocomposite film. *Carbohydr Polym*. 2012;90(4):1757-1763. doi:10.1016/j.carbpol.2012.07.065

106. Esposito Corcione C, Scalera F, Gervaso F, Montagna F, Sannino A, Maffezzoli A. One-step solvent-free process for the fabrication of high loaded PLA/HA composite filament for 3D printing. *J Therm Anal Calorim*. 2018;134(1):575-582. doi:10.1007/s10973-018-7155-5

107. Sithole MN, Kumar P, du Toit LC, Marimuthu T, Choonara YE, Pillay V. A 3D bioprinted in situ conjugated-co-fabricated scaffold for potential bone tissue engineering applications. *J Biomed Mater Res - Part A*. 2018;106(5):1311-1321. doi:10.1002/jbm.a.36333

108. Abouzeid RE, Khiari R, Beneventi D, Dufresne A. Biomimetic Mineralization of

Three-Dimensional Printed Alginate/TEMPO-Oxidized Cellulose Nanofibril Scaffolds for Bone Tissue Engineering. *Biomacromolecules*. 2018;19(11):4442-4452. doi:10.1021/acs.biomac.8b01325

109. Jessop ZM, Al-Sabah A, Gao N, et al. Printability of pulp derived crystal, fibril and blend nanocellulose-alginate bioinks for extrusion 3D bioprinting. *Biofabrication*. 2019;11(4). doi:10.1088/1758-5090/ab0631

110. Holback H, Yeo Y, Park K. 1 - Hydrogel swelling behavior and its biomedical applications. In: Rimmer S, ed. *Biomedical Hydrogels*. Woodhead Publishing Series in Biomaterials. Woodhead Publishing; 2011:3-24. doi:https://doi.org/10.1533/9780857091383.1.3

111. Siqueira P, Siqueira É, de Lima AE, et al. Three-dimensional stable alginate-nanocellulose gels for biomedical applications: Towards tunable mechanical properties and cell growing. *Nanomaterials*. 2019;9(1):1-22. doi:10.3390/nano9010078

112. Dodero A, Vicini S, Alloisio M, Castellano M. Sodium alginate solutions: correlation between rheological properties and spinnability. *J Mater Sci*. 2019;54(10):8034-8046. doi:10.1007/s10853-019-03446-3

113. Introduction I. IRCOBI Conference 2012. Published online 2012:2012.

114. Pailler-Mattei C, Bec S, Zahouani H. In vivo measurements of the elastic mechanical properties of human skin by indentation tests. *Med Eng Phys*. 2008;30(5):599-606. doi:10.1016/j.medengphy.2007.06.011

115. A K, A L. Mechanical Behaviour of Skin: A Review. *J Mater Sci Eng*. 2016;5(4). doi:10.4172/2169-0022.1000254

116. Müller M, Öztürk E, Arlov Ø, Gatenholm P, Zenobi-Wong M. Alginate Sulfate–Nanocellulose Bioinks for Cartilage Bioprinting Applications. *Ann Biomed Eng*. 2017;45(1):210-223. doi:10.1007/s10439-016-1704-5